



Wannier orbital theory and angle-resolved photoemission spectroscopy for the quasi-one-dimensional conductor $\text{LiMo}_6\text{O}_{17}$. I. Six-band t_{2g} Hamiltonian

L. Dudy 

Randall Laboratory, University of Michigan, Ann Arbor, Michigan 48109, USA;
Physikalisches Institut und Röntgen Center for Complex Material Systems, Universität Würzburg, D-97074 Würzburg, Germany;
and Synchrotron SOLEIL, L'Orme des Merisiers, 91190 Saint-Aubin, France

J. W. Allen 

Randall Laboratory, University of Michigan, Ann Arbor, Michigan 48109, USA

J. D. Denlinger 

Advanced Light Source, Lawrence Berkeley National Laboratory, Berkeley, California 94270, USA

J. He ^{*}


Department of Physics and Astronomy, Clemson University, Clemson, South Carolina 29534, USA

M. Greenblatt 

Department of Chemistry & Chemical Biology, Rutgers University, 123 Bevier Rd. Piscataway, New Jersey 08854, USA

M. W. Haverkort

Max-Planck-Institut für Festkörperforschung, Heisenbergstrasse 1, D-70569 Stuttgart, Germany;
Max-Planck-Institut für Chemische Physik fester Stoffe, Nöthnitzer Str. 40, D-01187 Dresden, Germany;
and Institut für Theoretische Physik, Universität Heidelberg, Philosophenweg 16, D-69120 Heidelberg, Germany

Y. Nohara and O. K. Andersen 

Max-Planck-Institut für Festkörperforschung, Heisenbergstrasse 1, D-70569 Stuttgart, Germany



(Received 19 March 2023; accepted 22 November 2023; published 21 March 2024)

In this and the two following papers, we present the results of a combined study by density-functional band theory and angle-resolved photoemission spectroscopy (ARPES) of lithium purple bronze, $\text{Li}_{1-x}\text{Mo}_6\text{O}_{17}$. This material is particularly notable for its unusually robust quasi-one-dimensional (quasi-1D) behavior. The band structure, in a large energy window around the Fermi energy, is basically two-dimensional and formed by three Mo t_{2g} -like extended Wannier orbitals (WOs), each one giving rise to a 1D band running at a 120° angle to the two others. A structural “dimerization” from $c/2$ to c gaps the xz and yz bands while leaving the xy bands metallic in the gap but resonantly coupled to the gap edges and, hence, to the two other directions. The resulting complex shape of the quasi-1D Fermi surface (FS), verified by our ARPES, thus depends strongly on the Fermi energy position in the gap, implying a great sensitivity to Li stoichiometry of properties dependent on the FS, such as FS nesting or superconductivity. The theory is verified in detail by the recognition and application of an ARPES selection rule that enables the separation in ARPES spectra of the two barely split xy bands and the observation of their complex split FS. The strong resonances prevent either a two-band tight-binding model or a related real-space ladder picture from giving a valid description of the low-energy electronic structure. Down to a temperature of 6 K we find no evidence for a theoretically expected downward renormalization of perpendicular single-particle hopping due to LL fluctuations in the quasi-1D chains. This paper I introduces the material, motivates our study, summarizes the N th-order muffin-tin orbital (NMTO) method that we use, analyzes the crystal structure and the basic electronic structure, and presents our NMTO calculation of the t_{2g} low-energy WOs and the resulting tight-binding Hamiltonian for the six lowest energy bands, only the four lowest being occupied. Thus this paper sets the theoretical framework and nomenclature for the following two papers.

DOI: [10.1103/PhysRevB.109.115143](https://doi.org/10.1103/PhysRevB.109.115143)

*Deceased.

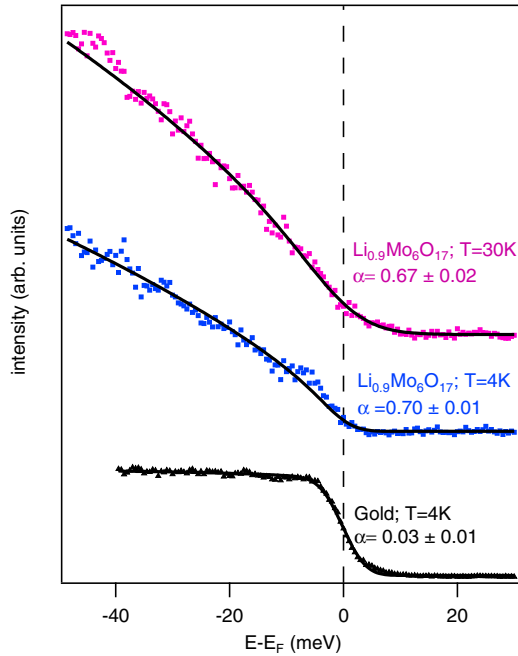


FIG. 1. Angle-integrated photoemission spectra of lithium purple bronze for $T = 4$ and 30 K taken with a resolution of 5 meV with photon energy $h\nu = 8.4$ eV [5]. For reference, a gold spectrum with the same settings is also shown. All the spectra are generally well fitted by the TL-model lineshape, showing for $\text{LiMo}_6\text{O}_{17}$ a value of $\alpha \approx 0.7$. In Ref. [5], it was deemed ambiguous whether a very noisy feature around 5 meV in the fit residuals is intrinsic or arises from some systematic experimental error. The gold spectrum fits well with α essentially zero, corresponding mathematically to a Fermi edge.

I. INTRODUCTION

The present paper I and its two companion papers II [1] and III [2] are devoted to a detailed study of the band structure of the lithium purple bronze (LiPB) $\text{LiMo}_6\text{O}_{17}$,¹ combining angle-resolved photoemission spectroscopy (ARPES) and Wannier function band theory using the N th-order muffin-tin orbital method (NMTO). Since its discovery [3] and structure determination [4] LiPB has been heavily studied as a quasi-one-dimensional (quasi-1D) material² [6–13]. Thus, it is notable as an unusually good and interesting example of the non-Fermi liquid (non-FL) properties exhibited by 1D interacting electron systems, such as in the exactly solvable Tomonaga-Luttinger (TL) model [14,15] or in the more generalized notion of the Luttinger liquid (LL) [16]. A highly nonintuitive example of such non-FL properties is that the energy E dependence of the momentum κ integrated single-particle spectral function, which would give simply the one-electron density of states in a noninteracting system, goes to zero upon approaching the Fermi-energy E_F as a power law

¹We do not use the conventional name, $\text{Li}_{0.9}\text{Mo}_6\text{O}_{17}$, because the highly accurate ARPES bands to be described here are filled corresponding to the stoichiometry $\text{Li}_{1.02}\text{Mo}_6\text{O}_{17}$ (see paper III [2]).

²Reference [5] summarizes and references prior work dating back to Ref. [3].

$(E_F - E)^\alpha$, with α interpreted as the anomalous exponent of the TL model.³

Figure 1 reproduces angle-integrated data from a previous photoemission study [5], showing this unusual property for LiPB for the spectral function below E_F , as probed by ARPES. The spectra for κ -integration along the quasi-1D direction, for temperatures $T = 4$ and 30 K and resolution 5 meV, are well described by a power law with $\alpha = 0.7$ over at least 40 meV, compared with the Fermi edge of a $T = 4$ K gold reference spectrum. Also, scanning tunneling spectroscopy [17], which probes the spectral function on both sides of E_F , shows the power law “V-shape” down to 4 K.⁴ It is then equally nonintuitive in the TL model that, nonetheless, the underlying band-structure Fermi momentum k_F and thus, the Fermi surface (FS) remains well defined [18]. Paper III presents a detailed determination of the FS for LiPB.

The band structure and, in particular, the magnitude(s) of the transverse hoppings (t_\perp) between its 1D chains, and the resulting FS, are especially interesting and important for LiPB. The general theoretical expectation [16] is that, for T decreasing below a scale set by t_\perp , LL behavior is unstable against dimensional crossover from 1D to some sort of three-dimensional (3D) Fermi-liquid (FL) behavior, typically by a phase transition to some 3D ordered state like a charge- or spin-density wave (CDW or SDW). Band calculations to date suggest values of $t_\perp = 20$ meV (232 K) and yet the data of Fig. 1 indicate that its non-FL 1D properties likely last until the material goes superconducting (SC) at $T_{SC} = 1.9$ K. Indeed, other properties of LiPB, albeit novel and interesting, exhibit no clear evidence for dimensional crossover above T_{SC} [5]. However, theory [16] also suggests that LL fluctuations on the chains can strongly suppress the single-particle hopping and consequently the crossover T . For example, in the case of one chain per primitive cell and hopping only to the nearest chain, the suppression of t_\perp is by the factor $(t_\perp/t)^{\alpha/(1-\alpha)}$, where $t \gg t_\perp$ is the hopping along the chains. For a typical band-theory value of $|t| = 0.8$ eV [19] and the value of $\alpha = 0.7$ cited above, one obtains $t_{\text{eff}\perp} = 4$ μeV or 0.04 K, even smaller than T_{SC} .⁵ Such a small value might thus account for the exceptional stability of 1D physics in this material and should be manifest in the low- T single-particle electronic structure. However, up to now, the transverse hopping and resulting FS have never been measured experimentally or characterized theoretically as fully as is needed and possible.

There is additional motivation for our study. As described in detail further below, LiPB is complex in having two approximately 1D bands associated with there being two equivalent chains (and two formula units) per primitive cell, each half filled for stoichiometric $\text{LiMo}_6\text{O}_{17}$. Thus most LiPB theories

³The power law is valid for $T = 0$. For nonzero T , the exact dependence evolves to be quantitatively more complicated but qualitatively similar.

⁴In Ref. [5], it was deemed ambiguous whether a very noisy feature around 5 meV in the fit residuals is intrinsic or arises from some systematic experimental error.

⁵Some measurements [20] have yielded a smaller $\alpha = 0.6$, for which the effective t_\perp is larger, 80 μeV or 0.9 K, still smaller than T_{SC} .

to date [6–9,11–13,19] have modeled the quasi-1D electrons as a lattice of pairs of chains regarded as ladders, with simple tight-binding (TB) t_{\perp} and t'_{\perp} parameters for nearest neighbor intra- and interladder hopping, respectively. So it is of great interest to check the validity of the ladder picture, which involves the relative magnitudes of the perpendicular hoppings within and between primitive cells. These hoppings determine the perpendicular dispersion and splitting of the two bands forming the FS. Of particular interest is the normal state FS giving rise to SC. The FS also gives the clearest experimental access to the details of the transverse hoppings.

Another motivation is to demonstrate the use of the NMTO method for creating chemically meaningful Wannier functions—in the present case Wannier orbitals (WOs) centered on Mo1, the only octahedrally fully coordinated molybdenum (Sec. III A)—and their TB Hamiltonian, and to establish them as important tools for predicting and interpreting the ARPES data. As summarized in more detail below, like the study in Ref. [21], our theory uses the local density-functional approximation (DFT-LDA) to derive a set of localized Wannier functions, which, however, in our case, is complete in the sense that it contains all three Mo1 $4d$ t_{2g} -like orbitals per formula unit, and thereby spans the occupied as well as the lowest empty bands. The two quasi-1D metallic bands are xy like and situated in a 0.4 eV gap between valence bands formed by the xz and yz WO, bonding between the ladder rungs, and conduction bands formed by the same WO, but antibonding between rungs. After integrating out the xz and yz degrees of freedom (in paper III [2]), our theory leads to the conclusions that the effective transverse couplings between the two quasi-1D bands cannot be described by a simple TB model and also that they have very long range, making ladders ill-defined. In this respect all previous TB ladder models are very unrealistic.

The theory also leads to a selection rule (in paper II [1]) that enables the two barely split quasi-1D bands to be separated in the ARPES spectra near E_F for the first time. The split and warped FS obtained thereby in ARPES at 6 K is in excellent agreement with the predicted FS, giving a detailed confirmation of the theory (paper III [2]). This means that the predicted LL renormalization of the perpendicular hoppings with decreased temperature does not occur and so cannot be the origin of the robustness of the LiPB 1D behavior. We can also infer that the LDA FS is the normal state FS relevant for theories [8,9,11,22,23] of the SC. We note that the occurrence of SC is sample dependent [24], and, in this context, that the details of the theoretical FS shape are extremely sensitive to the position of E_F , which is controlled by the Li content (or the content of oxygen vacancies). For our samples, the E_F position indicates that they are very nearly stoichiometric, which is the circumstance found in theory to give the most 1D FS. Although we have not explicitly verified SC for our samples, these findings are consistent with the hypothesis that SC has a 1D origin⁶ and that the absence of SC in some samples may be linked to sample stoichiometry through the

sensitivity of the FS. Finally, although T dependence was not a particular focus of the experiments, we find the *same* FS at 30 K, implying that a mysterious resistivity upturn below $T_M \approx 25$ K is not likely to be associated with a gross change in electronic structure [5].

Before proceeding we emphasize that our purpose is not merely to present the numerical results of yet another DFT-LDA calculation for LiPB. Rather, DFT-LDA is a tool to implement the overall program described in the three papers. We use it to obtain chemically meaningful NMTO WO, which, in turn, we use to gain new insight into how the numerical results come about. The central theory result is a portable six-band analytic TB Hamiltonian to describe the low-energy band structure. The agreement of its eigenvalues with the ARPES band structure is already generally good using LDA parameter values and can be made excellent by some additional adjustments, showing that its functional forms are faithful to the physics. Furthermore, along with its underlying WO, it can be used to understand the complex ARPES intensity variations in unprecedented detail, in particular the selection rule already mentioned. Ultimately, the combination of theory insight and ARPES experiment yields knowledge of the details of the Fermi surface and the magnitude and range of the perpendicular hopping for the two metallic bands.

In the remainder of this introductory section, we give a more detailed overview of the theory relative to previous work and describe the division of content between the three papers.

The basic band structure in the vicinity of E_F has been known for many years from pioneering TB calculations based on the semi-empirical extended Hückel method [26]. There are two approximately 1D bands dispersing across E_F , associated with there being two equivalent chains of Mo atoms having a zigzag arrangement (zig-Mo1-zag-Mo4-zig), and two formula units per primitive cell. The two bands have Mo $4d_{xy}$ character and for stoichiometric $\text{LiMo}_6\text{O}_{17}$ they are half filled. There are also two filled bands not far below E_F .

Quantitatively correct band structures require charge-self-consistent DFT calculations, not a small task for a transition-metal oxide with 48 atoms per cell, so it took nearly twenty years for the first self-consistent DFT (LDA) band structure to appear [27] and another six for the second [28]. Both calculations were performed with the linear muffin-tin orbital method (LMTO) in the atomic-spheres approximation. Such LDA-LMTO band structures provided guidance for the TB band-structure parameters used in early many-body models [6,19]. Higher-resolution low-temperature ARPES data and more accurate NMTO calculations show agreement even on the details [29] of the filled bands.

An alternative TB model [21] has been derived by first using the highly accurate full-potential linear augmented-plane-wave (LAPW) method to perform a charge self-consistent DFT (LDA) calculation of the band structure over a wide energy range, and then projecting from it a set of four so-called maximally localized Wannier functions, which describe the two quasi-1D bands and the two valence bands. The Wannier functions of this model are therefore not atomic but essentially the bonding linear combination of those on Mo1 and Mo4, and the integral for hopping between these xy -bond orbitals is only about half the one for hopping between the atomic orbitals considered in the TB models previously used [6,19]. The

⁶The SC upper critical field is much larger than the Pauli-limiting value [25], suggesting unconventional pairing arising from an essentially 1D normal state.

study of Nuss and Aichhorn [21] also provides a simplified two-band TB Hamiltonian by folding the two occupied xz and yz bands down into the two xy bands, thereby becoming $\tilde{x}\tilde{y}$ bands, and fitting their hybridization such as to modify the t_{\perp} parameters. The result is said to be in good agreement with those discussed in Ref. [19].

For the theory of the present paper and its two companion papers, early results of which were given in Ref. [29], we need and provide an improved 3D visualization of the crystal structure, with an associated wording (Sec. III of the present paper): ribbons containing Mo1, Mo2, Mo4, and Mo5 for zigzag chains and bi-ribbons for ladders, and an overview of the electronic structure (Sec. IV below). In the theory, we perform an LDA Wannier-function calculation with the new full-potential version [30] of the NMTO method. We obtain the set of all three (per formula unit) Mo1 $4d$ t_{2g} WOs, not only the xy orbitals, but also the xz and yz orbitals. Also the latter form 1D bands, but with primitive translations $(\mathbf{c} \pm \mathbf{b})/2$ until the dimerization to $\mathbf{c} \pm \mathbf{b}$ gaps them around E_F . Indeed (Sec. III A below), the structural reason why LiPB is 1D while (most) other Mo bronzes are two dimensional (2D) [31–34] is exactly this $c/2$ to c dimerization of the ribbons (zigzag chains) into bi-ribbons (the two zigzag chains are not related by translation). Note that this dimerization of the xz and yz bands causing them to gap at $2k_F$ is distinct from the $b/2$ to b dimerization causing the xy bands to gap at $4k_F$ —and which we neglect, as did Nuss and Aichhorn (Sec. III B below). Hybridization between the resulting valence and conduction bands and the metallic xy bands⁷ induces striking $k_{\perp} = k_c$ -dependent features [Fig. 7 below, Figs. II 10 (b) and 14 (c2), and Figs. III 3 and 8⁸]. These features depend strongly on the energy position in the gap. Therefore the resulting FS warping and splitting also has features that depend strongly on the value of E_F , as set by the effective Li stoichiometry. Furthermore, this E_F dependence of the perpendicular dispersion cannot be captured with a Wannier basis which, in addition to the metallic xy orbitals, contain only the *occupied* xz and yz orbitals [21]. We, therefore, include WOs which account not only for the valence but also for the conduction bands, leading to a very accurate and yet portable (i.e., analytical) t_{2g} six-band TB Hamiltonian. Subsequent analytical Löwdin downfolding to a two-band Hamiltonian, which has resonance rather than TB form, enables a new and detailed understanding of all the various microscopic contributions to the perpendicular dispersion and their relation to the crystal structure and to the FS.

The details of the theoretical method including all six Mo1 t_{2g} WOs and their TB Hamiltonian are presented in Secs. II, V, and VI of this paper. The theory of the ARPES intensity variations and its application to LiPB are presented in Sec. II of the following paper II [1], and the details of the downfolded two-band Hamiltonian and the resulting FS are presented in paper III [2]. The theory is validated in detail by new higher-resolution ARPES experiments for two different

samples, down to temperatures of 6 and 30 K. The data and the analysis results are presented at appropriate places in the course of the presentation of the theory in the three papers. As found previously [21,29], there is very good general agreement with LDA dispersions up to 150 meV below E_F . Refinement of the LDA-derived parameters of the six-band Hamiltonian yields an accurate and detailed description of the ARPES low-energy band structure (Sec. IV in paper II [1]), including the striking features of the xy -like bands and the associated distinctive FS features (Fig. 8 in paper III [2]). As mentioned already, the direct observation of these features, not identified in our previous ARPES studies, is enabled by the recognition and application of a selection rule (Sec. II in paper II [1]) according to which the c -axis dimerization gaps the energy bands, but—for a range of photon energies—has negligible effect on the ARPES intensities.

II. NTH-ORDER MUFFIN-TIN ORBITAL METHOD

The electronic-structure calculations were performed for the stoichiometric crystal with the structure determined for $\text{LiMo}_6\text{O}_{17}$ [4]. Doping—which is small due to the opposing effects of Li intercalation and O deficiencies—was treated in the rigid-band approximation.

For the DFT-LDA [35] calculations, including the generation of Wannier functions and their TB Hamiltonian, for the Kohn-Sham [36] one-electron energies $E_j^{\mathbf{k}}$ and eigenvectors, $u_{Rlm,j}^{\mathbf{k}}$, we used the recently developed self-consistent full-potential version [30] of the N th-order—also called third generation—muffin-tin orbital (NMTO) method [37,38], a descendant [39] of the classical linear muffin-tin orbital (LMTO) method [40,41]. Since NMTOs were hitherto generated for overlapping MT potentials imported from self-consistent LMTO-ASA or linear augmented plane wave (LAPW) calculations [42–52] rather than self-consistently in full-potential calculations, and since NMTO Wannier orbitals (WOs) are generated in a very different way than maximally localized Wannier functions [53], making them useful for many-body calculations also for d - and f -electron atoms at low-symmetry positions,⁹ here follows a concise description of our method as applied to LiPB. More complete and pedagogical accounts of the formalism may be found, e.g., in Refs. [38,39] and [55].

As illustrated in Chart (1), we first generate the full potential, $V(\mathbf{r})$, by charge self-consistent LDA calculation using a relatively large basis set $\chi_{Rlm}^{\mathbf{k}}(\mathbf{r})$ consisting of the Bloch sums of the two Li $2s$ NMTOs per primitive cell, of all 60 Mo $4d$ NMTOs, of all 136 O $2s$ and $2p$ NMTOs, plus 1381s

⁷We call the xy band the metallic band and, like for semiconductors, call the gapped xz and yz bands the valence and conduction bands.

⁸I, II, and III refer to sections, figures, and equations in papers I, II [1], and III [2], respectively.

⁹For materials with d - or f -electron atoms exclusively at high-symmetry positions, maximally localized and NMTO Wannier functions (WFs) give similar results when the settings are similar [45]. However, maximally localized WFs are usually not centered at low-symmetry sites and, if forced to, they generally do not transform according to the irreducible representations of the point group. As a consequence, crystal fields depend strongly on the settings. The software found on Ref. [54] interfaces several methods for generating WFs and allows users to compare results.

NMTOs on the interstitial sites (E) with MT radii exceeding 1 Bohr radius. The resulting number of 336 NMTOs/cell is smaller than the number of LMTOs [27,28]—and an order of magnitude smaller than the number of LAPWs [21] needed for LiPB.

Calculating $V(\mathbf{r})$ and $v_R(|\mathbf{r} - \mathbf{R}|)$ self-consistently using the LDA with the basis of 336 NMTOs/cell:

$$\begin{array}{ccc}
 H_{Rlm,R'l'm'}^k \& O_{Rlm,R'l'm'}^k & \rightarrow E_j^k \& u_{Rlm,j}^k \\
 \uparrow & Rlm & \downarrow \\
 E_{0,..,N} \& \chi_{Rlm}^k(\mathbf{r}) & \in & \rho(\mathbf{r}) \\
 \uparrow & 336 & \downarrow \\
 v_R(|\mathbf{r} - \mathbf{R}|) & \leftarrow & V(\mathbf{r}) \\
 \downarrow & & \downarrow \\
 (2) & & (2)
 \end{array} \quad (1)$$

After each iteration towards self-consistency, $V(\mathbf{r})$ is least-squared fitted to an *overlapping* MT potential (OMTP) [56], which is a constant, the MT zero, plus a superposition of spherically symmetric potential wells, $\sum_R v_R(|\mathbf{r} - \mathbf{R}|)$, centered at the atoms and larger interstitials. The ranges of the potential wells, the MT radii s_R , were chosen to overlap by 25%. Specifically: $s_{\text{Li}} = 2.87$, $s_{\text{Mo}} = 2.34\text{--}2.55$, $s_{\text{O}} = 1.72\text{--}1.89$, and $s_{\text{E}} = 1.03\text{--}2.48$ Bohr radii. The overlaps considerably improve the fit to the full potential and reduce the MT discontinuities of the potential and, hence, the curvatures of the basis functions.¹⁰ The OMTP is used to generate the NMTO basis set for the next iteration towards charge self-consistency and—this being reached—to generate the massively downfolded basis set consisting of the six Bloch sums of the Mo1 $4d(t_{2g})$ NMTOs which—after symmetrical orthonormalization and Fourier transformation (FT) (9) back to real space [see Chart (2)]—becomes the set of WOs describing the six bands around the Fermi level. The full potential $V(\mathbf{r})$ enables us to accurately include in the six-band TB Hamiltonian crystal-field terms, such as the one between the xy and the xz or the yz WOs which decisively influence the resonance peak in the metallic xy -like band (see Sec. II B 6 in paper III [2]).

Constructing the six WOs and their TB Hamiltonian:

$$\begin{array}{ccc}
 v_R(|\mathbf{r} - \mathbf{R}|) & \text{From (1)} & V(\mathbf{r}) \\
 \downarrow & \text{and Eq. (6)} & \downarrow \\
 E_{0,..,N} \& \chi_{Rlm}^k(\mathbf{r}) & \rightarrow H_{Rlm,R'l'm'}^k \& O_{Rlm,R'l'm'}^k \\
 & Rm \in 6 & \downarrow \\
 w_{Rm}(\mathbf{r} - \mathbf{R}) & \leftarrow \text{FT} & \chi^k(\mathbf{r}) (O^k)^{-\frac{1}{2}} \\
 \tilde{H}_{Rm,R'l'm'}^{TB} & \leftarrow \text{FT} & (O^k)^{-\frac{1}{2}} H^k (O^k)^{-\frac{1}{2}}
 \end{array} \quad (2)$$

We now describe the construction shown in Chart (3) of the NMTOs, which is more complex than that of, e.g., LAPWs but achieves order(s)-of-magnitude reduction in the size of the basis set. Admittedly, some understanding of solid-state chemistry is required to use NMTOs efficiently to generate WO sets, but they can provide insights not usually obtained by

use of plane-wave sets and projection of maximally localized Wannier functions [53].

Constructing the NMTO set:

$$\begin{array}{l}
 \text{Hard — sphere sites and radii } \mathbf{R}, a_R \\
 \text{OMTP wells and radii } v_R(r), s_R \approx 1.5a_R \\
 \text{Energy } E \text{ mesh } E_{0,..,N} \\
 \text{Radial wave functions } \varphi_{Rl}(E, r) \\
 \text{Phase shifts } \eta_{Rl}(E) \\
 \text{Partial waves } [\varphi_{Rl}(E, r) - \varphi_{Rl}^o(E, r)] Y_{lm}(\hat{\mathbf{r}}) \\
 \text{Screened spherical waves } \psi_{Rlm}(E, \mathbf{r}) \\
 \text{Screened structure (or slope) matrix } S_{R'l'm', Rlm}(E) \\
 \text{Kinked partial waves } \phi_{Rlm}(E, \mathbf{r}), \text{ Eq. (4)} \\
 \text{Kink matrix } K_{R'l'm', Rlm}(E), \text{ Eq. (5)} \\
 \text{Downfolding from } K^{336}(E) \text{ to } K^6(E), \text{ Eq. (6)} \\
 \text{Green matrix } G(E) = K(E)^{-1} \\
 \text{Lagrange matrix } L_{Rlm,R'l'm'}(E_v) \\
 \text{NMTOs } \chi_{Rlm}(\mathbf{r}), \text{ Eq. (7)} \\
 \text{Overlap matrix } \langle \chi_{Rlm}^k | \chi_{R'l'm'}^k \rangle \equiv O^k \\
 \text{Hamiltonian matrix } \langle \chi_{Rlm}^k | -\Delta + V(\mathbf{r}) | \chi_{R'l'm'}^k \rangle \equiv H^k
 \end{array} \quad (3)$$

For each MT well $v_R(r)$ and energy E on an $(N + 1)$ point mesh, the radial Schrödinger equations¹¹ for $l = 0, \dots, l_{R\text{max}}$ are integrated outwards from the origin to the MT radius, s_R , thus yielding the radial functions, $\varphi_{Rl}(E, r)$, and their phase-shifts, $\eta_{Rl}(E)$, which due to the centrifugal term vanish for all $l \geq l_{\text{max}}(R)$. Continuing the integration smoothly inwards—this time over the MT zero—yields the phase-shifted free waves $\varphi_{Rl}^o(E, r)$, which we truncate at and inside the so-called *hard* sphere with radius $a_R \approx 0.65s_R$. The differences $\varphi_{Rl}(E, r) - \varphi_{Rl}^o(E, r)$, often referred to as *tongues*, tend smoothly to zero when going outside the MT sphere and jump discontinuously to $\varphi_{Rl}(E, r)$ when going inside the hard sphere. After multiplication by the appropriate cubic harmonic $Y_{lm}(\hat{\mathbf{r}})$, these *discontinuous and tongued partial waves* will be used together with the screened spherical waves (SSWs) $\psi_{Rlm}(E, \mathbf{r})$, to be defined below, to form a set of *kinked partial waves* (KPWs),¹² $\phi_{Rlm}(E, \mathbf{r})$, analogous to Slater's augmented plane waves (APWs), and—eventually—of smooth and energy-independent NMTOs [see Eqs. (4) and (7)]. Partial waves with the same Rlm as one of the NMTOs in the basis set are called *active* (A) and the remaining partial waves with nonzero phase shifts are called *passive*. Since $l_{\text{max}}(R) = 4, 3, 3$, and 2 for $R = \text{Mo}, \text{O}, \text{Li}$, and E , the vast majority of partial waves are passive.

¹⁰The LMTOs of Methfessel and Schilfgaard [57] are defined for a conventional MT potential but are modified in the interstitial near the MTs to avoid large discontinuities of the orbital curvatures. Also, the LMTOs of Wills *et al.* [58–60] are defined for MTs without overlap but are not modified. As a consequence, multiple- κ sets are needed.

¹¹Actually, the scalar-relativistic Dirac equations.

¹²KPWs are also called exact, energy-dependent MTOs (EMTOs) [61,62].

To combine the many partial waves to the set of KPWs, we first form the set of *tail* or *envelope* functions $\psi_{Rlm}(E, \mathbf{r})$, also called *screened spherical waves* (SSWs): They are wave-equation solutions that satisfy the boundary conditions that any cubic-harmonic projection around any site, $\hat{P}_{R'l'm'}(r_R)\psi_{Rlm}(E, \mathbf{r})$, has a node at the hard-sphere radius if $R'l'm'$ is active and differs from Rlm , and has the proper phase shift $\eta_{R'l'}(E)$ if $R'l'm'$ is passive. This node condition is what makes the SSW localized—and the more, the larger the basis set, i.e., the number of active channels. The input to a screening calculation (see Sec. 3.3 in Ref. [55] or Sec. II B in Ref. [30]) is the energy, the hard-sphere structure, and the passive phase shifts. The output is the *screened structure* or *slope matrix* whose element $S_{R'l'm',Rlm}(E)$ gives the slope of $\psi_{Rlm}(E, \mathbf{r})$ at the hard sphere in the active $R'l'm'$ channel. The set of screened spherical waves is then augmented by the partial waves to become the basis set of KPWs (see, e.g., Figs. 4–6 in Ref. [55]):

$$\phi_{Rlm}(E, \mathbf{r}) = \psi_{Rlm}(E, \mathbf{r}) + [\varphi_{Rl}(E, r) - \varphi_{Rl}^o(E, r)]Y_{lm}(\hat{\mathbf{r}}). \quad (4)$$

The KPW $\phi_{Rlm}(E, \mathbf{r})$ has a head formed by the active partial wave with the *same* Rlm , plus passive waves, and a tail which inside the other MT spheres is formed solely by passive partial waves. Hence, all active projections of $\phi_{Rlm}(E, \mathbf{r})$, except its own, vanish. Such a KPW is localized, everywhere continuous, and everywhere a solution of Schrödinger's equation for the MT potential—*except* at all hard spheres where it has *kinks* in the active channels. The kink, $K_{R'l'm',Rlm}(E)$, at the hard sphere in channel $R'l'm'$ is

$$S_{R'l'm',Rlm}(E) - \delta_{R'l'm',Rlm} \left. \frac{\partial \ln \varphi_{Rl}^o(E, r)}{\partial \ln r} \right|_{a_R}. \quad (5)$$

This kink matrix also equals the MT Hamiltonian minus the energy, i.e., the kinetic energy, in the KPW representation: $K(E) = \langle \phi(E) | -\Delta + \sum_R v_R - E | \phi(E) \rangle$. Any linear combination of KPWs with the property that the kinks from all heads and tails cancel is smooth and therefore, by construction, a solution with energy E of Schrödinger's equation for the OMTP—except for the tongues sticking into neighboring MT spheres and thereby causing errors of merely second and higher order in the potential overlap. This kink-cancellation condition gives rise to the screened Korringa-Kohn-Rostoker (KKR) *secular* equations of band theory: $K(E)u = 0$.

Downfolding of a large to a small set of KPWs corresponds to changing the phase shifts in the channels to be downfolded (denoted I for “integrated out”) from those of hard spheres, $\eta_A(E)$, to the proper phase shifts, $\eta_{Rl}(E)$, and is performed on the kink matrix (5). An example is the kink matrix for the set of six KPWs in terms of the blocks of the kink matrix for the 336 set:

$$K_{AA}^6(E) = K_{AA}^{336}(E) - K_{AI}^{336}(E)K_{II}^{336}(E)^{-1}K_{IA}^{336}(E). \quad (6)$$

Note that this downfolding, which is done *prior* to N -ization (7) (see Chart (3)), makes the resulting NMTO set far better localized and far more accurate than the set obtained by standard Löwdin downfolding of a basis of energy-independent orbitals, e.g., LMTOs [63], Slater type orbitals [64], or NMTOs, followed by linearization of the energy dependence of the denominators [e.g. Eq. (4) in paper III [2]].

For a *Hamiltonian* formulation of the band-structure problem, we need a basis set of energy-independent *smooth* functions analogous to the well-known *linear* APWs (LAPWs) and MTOs (LMTOs) [40]. This set [37–39] is arrived at by N th-order polynomial interpolation (Lagrange) in the Hilbert space of KPWs with energies at a chosen mesh of $N + 1$ energies E_0, \dots, E_N :

$$\chi_{R'l'm'}(\mathbf{r}) = \sum_{v=0}^N \sum_{Rlm}^{\text{active}} \phi_{Rlm}(E_v, \mathbf{r}) L_{Rlm, R'l'm'}(E_v). \quad (7)$$

Here, $\chi_{R'l'm'}(\mathbf{r})$ is a member of the active set of NMTOs and $L(E_v)$ is the matrix of Lagrange coefficients, which is given by the kink matrix (5) evaluated at the points of the energy mesh. For an NMTO, the kinks at the hard spheres are reduced to discontinuities of the $(2N + 1)$ st derivatives and for a quadratic ($N = 2$) MTO (QMTO), as used for LiPB, this means that the four lowest radial derivatives are continuous, i.e., the QMTO is “supersmooth.” Also the MT-Hamiltonian- and overlap matrices in the NMTO representation, $H = \langle \chi | -\Delta + \sum_R v_R | \chi \rangle$ and $O = \langle \chi | \chi \rangle$, are given by the kink matrix and its first energy derivative evaluated at the energy mesh—or more conveniently—as divided differences of its inverse, the Green matrix $G(E) \equiv K(E)^{-1}$ [see Eqs. (91), (94), and (95) in Ref. [39]].

The NMTO set may be arbitrarily small and, nevertheless, span the exact solutions at the $N + 1$ chosen energies of Schrödinger's equation for the MT potential to first order in the potential overlap. Specifically, a set with n NMTOs (per cell) yields n eigenfunctions and eigenvalues (energy bands) E whose errors are proportional to, respectively, $(E - E_0) \times \dots \times (E - E_N)$ and $(E - E_0)^2 \times \dots \times (E - E_N)^2$. The choice of NMTO set, i.e., which orbitals to place on which atoms, merely determines the prefactors of these errors and the range of the orbitals. But only with chemically sound choices will the delocalization of the KPWs caused by the N -ization in Eq. (7) be negligible.

To explain this, we now consider the simple example of NaCl-structured NiO: Placing the three p orbitals on every O, the five d orbitals on every Ni, and letting the energy mesh span the 10 eV region of the pd bands generates a basis set of eight atomic-like NMTOs yielding the eight pd bands and wave functions [see Figs. 2 and 4 in Ref. [52] and Fig. 7 (top) in Ref. [55]]. Placing merely the three p orbitals on every O and letting the mesh span the 5 eV region of the O p bands generates a basis set consisting of O p -like NMTOs with bonding d -like tails on the Ni neighbors, which yields accurate p bands and wave functions [Fig. 7 (bottom) in Ref. [55]]. Placing, instead, the five d orbitals on every Ni and letting the mesh span the 4 eV region of the Ni d bands generates a basis set of Ni d -like NMTOs which have antibonding p -like tails on the O neighbors and yields accurate d -bands and wave functions [Fig. 7 (center) in Ref. [55]]. With the five d orbitals on Ni, *but* a mesh spanning the three O p bands, we get three $d(t_{2g})$ -like Ni NMTOs xy , xz , and yz with large $pd\pi$ -bonding p tails on the four O neighbors in the plane of the t_{2g} orbital, plus the two $d(e_g)$ -like Ni NMTOs with huge $pd\sigma$ -bonding tails—on the two apical oxygens for $3z^2 - 1$, and on the four oxygens in the xy plane for $x^2 - y^2$. These fairly delocalized Ni d NMTOs clearly exhibit the Ni-O

bonding, but they form a schizophrenic basis set which yields the three $O\ p$ bands connected across the pd gap to two of the five $Ni\ d$ bands by steep “ghost” bands.

This example indicates how the NMTO method can be used to explore covalent interactions in complex materials. Other examples may be found in Refs. [42–52]. Note that the fewer the bands to be picked out of a manifold, i.e., the more diluted the basis set, the more extended are its orbitals because the set is required to solve Schrödinger’s equation in all space. The increased extent leads to an (exponentially) increased energy dependence of the KPWs and that requires using NMTOs with a finer energy mesh. As a consequence, the smaller the set, the more complicated its orbitals.

Generalized Wannier functions are finally obtained by orthonormalization of the corresponding NMTO set [see Chart (2)]. *Symmetrical orthonormalization* yields the set of Wannier functions, which we refer to as *Wannier orbitals* (WOs) because they are atom-centered with specific orbital characters. The localization of these WOs hinges on the fact that each KPW in the set vanishes (with a kink) inside the hard sphere of any other KPW in the set. This condition essentially maximizes the on-site and minimizes the off-site Coulomb integrals and has the same spirit as the condition of minimizing the spread, $\langle \chi || \mathbf{r} - \mathfrak{R} |^2 | \chi \rangle$, used to define the maximally localized Wannier functions [53].

For LiPB, we used quadratic $N(=2)$ MTOs and for the large-basis-set calculation chose the three energies $E_v = \pm 1$ and 0 Ry with respect to the MT zero, i.e., -22 , -8 , and 6 eV with respect to the center of the gap, which is approximately the Fermi level (see Fig. 3). For the six-orbital calculation, we took $E_v = -0.8$, -0.4 , and 0.2 eV with respect to the center of the gap (see Fig. 12 in paper II [1]).

For the low-energy electronic structure of $\text{LiMo}_6\text{O}_{17}$ we need to pick from the sixty Mo $4d$ bands above the $O\ 2p$ —Mo $4d$ gap (see Fig. 3) a conveniently small and yet separable set of bands around the Fermi level. In this case, where no visible gap separates such bands from the rest of an upwards-extending continuum, the NMTO method is uniquely suited for picking a subset of bands for which the Wannier set is intelligible and as localized as possible. This *direct generation* of WOs (through trial and error by inspecting the resulting bands like we discussed above for NiO) differs from the procedures for projecting localized Wannier functions from the Bloch functions of the computed band structure by judiciously choosing their phases [65,66] or by minimizing the spread [21,53]. We shall return to it in Sec. V after the crystal structure and the basic electronic structure of LiPB has been discussed.

Since the resulting set of six NMTOs may have a fairly long range, all LDA calculations were performed in the representation of Bloch sums,

$$\chi_{Rm}(\mathbf{k}, \mathbf{r}) \equiv \sum_{\mathbf{T}} \chi_{Rm}(\mathbf{r} - \mathbf{T}) e^{2\pi i \mathbf{k} \cdot \mathbf{T}}, \quad (8)$$

of orbitals translated by the appropriate lattice vector \mathbf{T} . Specifically, the screening of the structure matrix was done \mathbf{k} -by- \mathbf{k} . To obtain printable WOs—obtained by symmetrical orthonormalization of the NMTOs—and a portable Hamiltonian whose $H_{R'm', R+Tm}$ element is the integral for hopping between the WOs centered at, respectively, \mathbf{R}' and $\mathbf{R} + \mathbf{T}$, we

need to Fourier transform back to real space:

$$H_{R'm', R+Tm} = |\mathbf{a} \cdot \mathbf{b} \times \mathbf{c}| \int_{\text{BZ}} d^3k e^{-2\pi i \mathbf{k} \cdot \mathbf{T}} H_{R'm', Rm}(\mathbf{k}). \quad (9)$$

Here, the integral with its prefactor is the average over the BZ, as is appropriate when the localized orbital is normalized to unity. Moreover, $H_{Rm', Rm}$ is the energy of the orbital when $m = m'$, and the crystal-field term when $m \neq m'$. The Hamiltonian (9), truncated after $|\mathbf{R} - \mathbf{R}' - \mathbf{T}|$, exceeds some distance, the lattice constant a for LiPB, we shall refer to as the *tight-binding* (TB) Hamiltonian (Sec. VI). This truncation makes its energy-band eigenvalues more smooth and wavy than those of $H_{R'm', Rm}(\mathbf{k})$.

To the MT Hamiltonian, we finally add the second-order correction for the tongue-overlap and the full-potential perturbation [39,67]. Products of NMTOs—as needed for evaluation of matrix elements and the charge density—are evaluated as products of partial waves limited to their MT spheres plus products of screened spherical waves [39,55]. The latter are smooth functions and are interpolated across the interstitial from their first three radial derivatives at the hard sphere [30]. To make it trivial to solve Poisson’s equation, this interpolation uses spherical waves which—in order to make the matching at the hard spheres explicit—are screened to have all phase shifts with $l \leq 4$ equal to those of hard spheres.

The band structure obtained from our full-potential LDA calculation with the large NMTO basis set agrees well with LDA and GGA control calculations performed with the LAPW method. We did not include the spin-orbit coupling in the NMTO calculation, but did so with the LAPW method and show the result in paper II [1], Fig. 13, together with the LDA TB bands.

III. CRYSTAL STRUCTURE

The crystal structure of LiPB was determined at room temperature and described by Onoda *et al.* [4]. As shown in Fig. 2, there are two $\text{LiMo}_6\text{O}_{17}$ units in the primitive cell spanned by the translations \mathbf{a} , \mathbf{b} , and \mathbf{c} shown in Fig. 2(a). Whereas \mathbf{b} is orthogonal to both \mathbf{c} and \mathbf{a} , the latter has a tiny component along \mathbf{c} . The relative lengths of the primitive translation vectors are $a/b \approx 2.311$ and $c/b \approx 1.720$, with $b = 5.523$ Å. We note that, in much of the literature, especially experimental papers, an alternate axis labeling [3] is used¹³ with the definitions of a and c interchanged. Here we follow Onoda *et al.* [4]. Since \mathbf{a} , \mathbf{b} , and \mathbf{c} are nearly orthogonal, so are the primitive translations, \mathbf{a}^* , \mathbf{b}^* , and \mathbf{c}^* , of the reciprocal lattice. They are defined by

$$\begin{pmatrix} \mathbf{a} \cdot \mathbf{a}^* & \mathbf{a} \cdot \mathbf{b}^* & \mathbf{a} \cdot \mathbf{c}^* \\ \mathbf{b} \cdot \mathbf{a}^* & \mathbf{b} \cdot \mathbf{b}^* & \mathbf{b} \cdot \mathbf{c}^* \\ \mathbf{c} \cdot \mathbf{a}^* & \mathbf{c} \cdot \mathbf{b}^* & \mathbf{c} \cdot \mathbf{c}^* \end{pmatrix} \equiv \begin{pmatrix} 1 & 0 & 0 \\ 0 & 1 & 0 \\ 0 & 0 & 1 \end{pmatrix}, \quad (10)$$

where we use the *crystallographic* definition of the scale of reciprocal space without the factor 2π on the right-hand side used in the *solid-state* definition. The former is traditionally used in diffraction and the latter in spectroscopy. In this paper,

¹³It is, therefore, essential to check any particular article for these definitions.

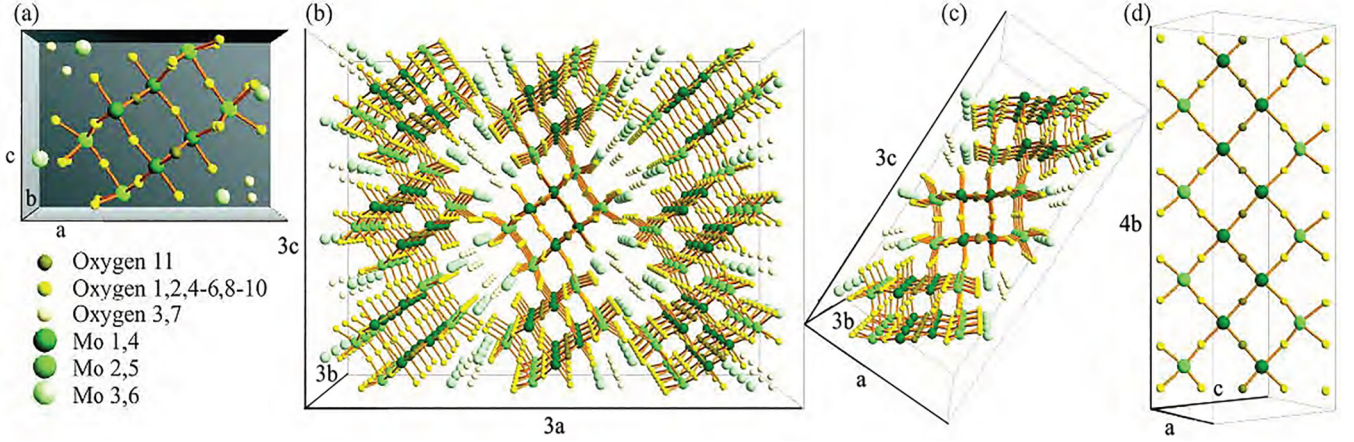


FIG. 2. Crystal structure of $\text{LiMo}_6\text{O}_{17}$. Li (not shown) is intercalated in the hollows near light-green Mo and light-yellow O atoms. (a) Primitive cell spanned by the translation vectors \mathbf{a} , \mathbf{b} , and \mathbf{c} . Whereas \mathbf{b} is orthogonal to both \mathbf{c} and \mathbf{a} , the latter has a one-percent component along \mathbf{c} . The relative lengths of the translation vectors are $a/b \approx 2.31$ and $c/b \approx \sqrt{3}$. The primitive cell contains two strings: (Mo3) - Mo2 - Mo1 - Mo4 - Mo5 - (Mo6) and the inverted one (MO6) - MO5 - MO4 - MO1 - MO2 - (MO3). When we need to distinguish between two equivalent sites (related by inversion), we use upper-case letters for the one in the upper string. Together, the two strings form a bistring. (b) A $3 \times 3 \times 3$ supercell showing bc slabs translated by $\pm \mathbf{a}$. The slabs are separated by Mo3 and Mo6 (light green). (c) A single slab, rotated such that sixfold-coordinated Mo (green and dark green) have their bonds to O in the vertical z and two horizontal x and y directions Eq. (12). Oriented this way, see also Chart (14), the slab forms a staircase running up the c direction, i.e., with the steps translated by \mathbf{c} . A single step is a bi-ribbon formed by translating a bistring infinitely many times by \mathbf{b} . The midpoint between Mo1 and a nearest MO1 in the same bi-ribbon is a center of inversion. The planes perpendicular to \mathbf{b} containing Mo1 and Mo5, as well as those containing Mo4 and Mo2, are mirror planes. The sequence along the vertical, almost straight lines along \mathbf{z} is (MO6) - Mo5 - MO2 - Mo1 - MO4 - (Mo3) and Li intercalates between the Mo_3O_4 tetrahedron and the MO_3O_4 tetrahedron right above it [4]. (d) Four primitive cells along b of a single ribbon. Along its center runs the dark-green Mo_1/Mo^4 zigzag chain. Parallel herewith and shifted by \mathbf{z} [see panel (c) and Charts (14)–(15)] is the partner ribbon with its MO_4/MO^1 zigzag chain (see also Fig. 1 in Ref. [27]).

we use the crystallographic definition unless otherwise stated. The top of Fig. 3 shows half the Brillouin-zone (BZ) with origin at Γ and spanned by $\pm \mathbf{a}^*/2$ (B), $\pm \mathbf{b}^*/2$ (Y), and $\pm \mathbf{c}^*/2$ (Z). The Bloch vector,

$$\mathbf{k} = k_a \mathbf{a}^* + k_b \mathbf{b}^* + k_c \mathbf{c}^*, \quad (11)$$

is specified by its dimensionless (k_a, k_b, k_c) components which, according to Eqs. (10) and (11), are the projections of \mathbf{k} onto, respectively, \mathbf{a} , \mathbf{b} , and \mathbf{c} , or, equivalently, they are the projections onto the respective *directions* in units of a^{-1} , b^{-1} , and c^{-1} . Occasionally we shall use the solid-state definition where the k components are the same but \mathbf{a}^* , \mathbf{b}^* , \mathbf{c}^* , and \mathbf{k} are 2π larger, e.g., the Fermi vector for stoichiometric LiPB has length $(\pi/2)b^{-1} = 0.2844 \text{ \AA}^{-1}$ instead of $(1/4)b^{-1}$.

The most relevant symmetry points have $k_a = 0$, and are $(k_b, k_c) = Z(0, \frac{1}{2})$, $Y(\frac{1}{2}, 0)$, $\Gamma(0, 0)$, $C(\frac{1}{2}, \frac{1}{2})$, $W(\frac{1}{2}, \frac{1}{4})$, $\Lambda(0, \frac{1}{4})$, plus their equivalents. Higher BZs are shifted by reciprocal-lattice vectors \mathbf{G} , which means that k_a , k_b , and k_c are shifted by integers, which we name, respectively, L , M , and N and shall use in Sec. VI and in Secs. II B and III C in paper II.

A simplifying *approximate* view of the complicated structure in Fig. 2 is that all Mo atoms are on a lattice spanned by the primitive translations:

$$\frac{\mathbf{c} + \mathbf{a}}{6} \mp \frac{\mathbf{b}}{2} \equiv \frac{\mathbf{x}}{\mathbf{y}} \quad \text{and} \quad \frac{\mathbf{c}}{2} - \frac{\mathbf{c} + \mathbf{a}}{6} \equiv \mathbf{z}. \quad (12)$$

These are orthogonal to within a few degrees and their lengths 3.82 \AA are equal to within 0.3%. This means that all 12 Mo

atoms approximately form a simple cubic lattice, 12 times finer than the proper lattice. In Fig. 2(c), the structure is turned to have \mathbf{z} in the vertical direction and \mathbf{x} and \mathbf{y} in the horizontal plane. This view is useful for understanding the structure, the computed Wannier orbitals, and the measured ARPES, but should not be overstretched. Using, for instance, the inverse to the transformation (12),

$$\mathbf{a} = 2(\mathbf{x} + \mathbf{y} - \mathbf{z}), \quad \mathbf{b} = \mathbf{y} - \mathbf{x}, \quad \mathbf{c} = \mathbf{x} + \mathbf{y} + 2\mathbf{z}, \quad (13)$$

and assuming the xyz system to be orthonormal leads to $a = 2\sqrt{3}$, $b = \sqrt{2}$, and $c = \sqrt{6}$ times 3.82 \AA , which are wrong by, respectively, $+3.7\%$, -2.2% , and -2.1% .

As specified in Fig. 2(a), of the twelve Mo sites in the primitive cell, six are inequivalent. Four of these (dark-green Mo1 and Mo4, and green Mo2 and Mo5) are sixfold coordinated with oxygen (dark yellow and yellow) in the $\pm x$, $\pm y$, and $\pm z$ directions and form a network of *corner-sharing* MoO_6 octahedra. We call them octahedral molybdenums. The remaining two types of Mo (light-green Mo3 and Mo6) are fourfold coordinated with oxygen (yellow and light yellow). The latter, *tetrahedrally* coordinated Mo atoms (light green, set in parentheses in the following) form double layers, which separate the network of corner-sharing MoO_6 octahedra into *slabs*. The crystals cleave between slabs.

Such a slab has the form of a *staircase* with steps of *bi-ribbons* stacked with period \mathbf{c} as seen in Fig. 2(c). Schemat-

ically, this is

$$\begin{array}{c}
 \mathbf{c} \nearrow \\
 \mathbf{a} \nearrow \\
 \mathbf{z} \uparrow
 \end{array}
 \begin{array}{|c|c|c|c|c|c|}
 \hline
 \mathbf{2} & \mathbf{1} & \mathbf{4} & \mathbf{5} & \mathbf{2} & \mathbf{1} & \mathbf{4} \\
 \hline
 \mathbf{1} & \mathbf{2} & & \mathbf{5} & \mathbf{4} & \mathbf{1} & \mathbf{2} \\
 \hline
 \mathbf{4} & \mathbf{5} & & \mathbf{2} & \mathbf{1} & \mathbf{4} & \mathbf{5} \\
 \hline
 & & \mathbf{5} & \mathbf{4} & \mathbf{1} & \mathbf{2} & \mathbf{5} \\
 \hline
 & & \mathbf{2} & \mathbf{1} & \mathbf{4} & \mathbf{5} & \mathbf{2} \\
 \hline
 \mathbf{5} & \mathbf{4} & \mathbf{1} & \mathbf{2} & \mathbf{5} & \mathbf{4} & \mathbf{1} \\
 \hline
 \mathbf{2} & \mathbf{1} & \mathbf{4} & \mathbf{5} & \mathbf{2} & \mathbf{1} & \mathbf{4} \\
 \hline
 \end{array}, \quad (14)$$

where the octahedral molybdenums lying in the same ac plane are either normal- or boldfaced. The distance between such ac planes is $\mathbf{b}/2$. A *single ribbon* is four octahedral molybdenums *wide* and, as seen here,

$$\begin{array}{c}
 \mathbf{b} \uparrow \\
 \mathbf{c} + \mathbf{a} \rightarrow \\
 \mathbf{y} \nearrow \\
 \mathbf{x} \searrow
 \end{array}
 \begin{array}{|c|c|}
 \hline
 \text{Mo :} \\
 \hline
 \mathbf{2} & \mathbf{4} \\
 \hline
 \mathbf{1} & \mathbf{5} \\
 \hline
 \mathbf{2} & \mathbf{4} \\
 \hline
 \mathbf{1} & \mathbf{5} \\
 \hline
 \mathbf{2} & \mathbf{4} \\
 \hline
 \mathbf{1} & \mathbf{5} \\
 \hline
 \end{array},
 \begin{array}{|c|c|}
 \hline
 \text{MO :} \\
 \hline
 \mathbf{5} & \mathbf{1} \\
 \hline
 \mathbf{4} & \mathbf{2} \\
 \hline
 \mathbf{5} & \mathbf{1} \\
 \hline
 \mathbf{4} & \mathbf{2} \\
 \hline
 \mathbf{5} & \mathbf{1} \\
 \hline
 \mathbf{4} & \mathbf{2} \\
 \hline
 \end{array}, \quad (15)$$

and in Figs. 2(c) and 2(d) extends indefinitely in the b direction and lies in the horizontal xy plane containing the vectors $\mathbf{b} = \mathbf{y} - \mathbf{x}$ and $\mathbf{c} + \mathbf{a} = 3(\mathbf{x} + \mathbf{y})$. The lower half of a bi-ribbon, seen in the left-hand panel of Chart (15), consist of (Mo3) - Mo2 - Mo1 - Mo4 - Mo5 - (Mo6) *strings* separated by \mathbf{b} and can be taken either as a zigzag line changing translation between \mathbf{y} and \mathbf{x} , and thus running along $\mathbf{c} + \mathbf{a}$, or as a nearly straight line running along \mathbf{x} , or as one running along \mathbf{y} [see Fig. 2(d) and Chart (15)]. In the following, we refer to these as, respectively, $(\mathbf{c} + \mathbf{a})$ zigzags, \mathbf{x} strings, and \mathbf{y} strings.

The *upper ribbon* is shown to the right in Chart (15). Its Mo sequence, (MO6) - MO5 - MO4 - MO1 - MO2 - (MO3), is *inverted* such that, e.g., MO4 is on top of Mo1. When we *need* to distinguish between two equivalent sites related by inversion in their midpoint—a center of inversion for the entire crystal—we use uppercase letters for the one in the upper ribbon.

Note that the $(\mathbf{c} + \mathbf{a})$ -zigzag string is different from – and perpendicular to – the $\backslash_{\text{Mo1}}^{\text{Mo4}} \backslash$ zigzag chain along \mathbf{b} , the backbone of the electronic 1D xy band shown in Fig. 1 of Ref. [27] together with its partner $\backslash_{\text{MO4}}^{\text{MO1}} \backslash$ in the upper ribbon.

A. c dimerization

The vectors from Mo1 to its two nearest MO1 neighbors inside and outside the bi-ribbon are, respectively, $(\mathbf{c} \pm \mathbf{b})/2 - \mathbf{d}$ and $-(\mathbf{c} \pm \mathbf{b})/2 + \mathbf{d}$, where

$$\mathbf{d} = 0.012\mathbf{a} + 0.033\mathbf{c} \quad (16)$$

is the *displacement dimerization*. Hence, the distances measured along \mathbf{c} from a ribbon to its neighbors inside and outside the bi-ribbon are, respectively, 6.6% smaller and 6.6% larger than the average distance $c/2$.

Due to the stacking (14) into a staircase of bi-ribbons, Mo4 differs from Mo1, and Mo5 differs from Mo2, in having *no* neighbor belonging to the next bi-ribbon, i.e., they have only *one* octahedral Mo neighbor along z . As seen in Charts (14)

and (15), Mo1 has six, Mo4 five, Mo2 four, and Mo5 three nearest Mo neighbors which are octahedrally coordinated with oxygen.

In the next section, we shall explain—and later demonstrate by computation and experiment—that the six lowest energy bands are described by the six *planar* t_{2g} Wannier orbitals (WOs), $w_m(\mathbf{r})$ and $W_m(\mathbf{r})(m = xy, xz, yz)$, centered¹⁴ on, respectively, Mo1 and on MO1. These sites, separated by $(\mathbf{c} + \mathbf{b})/2 - \mathbf{d}$, are *special* in having a *full* nearest-neighbor shell of octahedral molybdenums and therefore best preserve the t_{2g} symmetry of the WO and are least sensitive to the *steps* of the staircase of the WO and are least sensitive to the *dimerization*. Such a WO (Fig. 9) spreads substantially onto the four nearest Mo neighbors in the orbital's plane with amplitudes falling in the same order as the above-mentioned Mo coordination of those neighbors. As a result of this, and the smallness of the displacement dimerization (16), the two $t_{2g,m}$ WO are *approximately* related by *half* a lattice translation:

$$W_m\left(\mathbf{r} - \frac{\mathbf{c} + \mathbf{b}}{2}\right) \approx w_m(\mathbf{r}). \quad (17)$$

However, the *exact* relation is

$$W_m\left(\mathbf{r} - \frac{\mathbf{c} + \mathbf{b}}{2} + \mathbf{d}\right) = w_m(-\mathbf{r}), \quad (18)$$

and its differences, $W_m(\mathbf{r} - \frac{\mathbf{c} + \mathbf{b}}{2} + \mathbf{d}) - W_m(\mathbf{r} - \frac{\mathbf{c} + \mathbf{b}}{2})$ and $w_m(-\mathbf{r}) - w_m(\mathbf{r})$, to the approximate relation (17), will be referred to as, respectively, the *displacement* and the *inversion dimerization*.

A consequence of the approximate translational equivalence (17), which may be seen to hold far better for the xy than for the xz and yz WO, is that the low-energy band structure, $E_j(\mathbf{k})$ with $j = 1-6$ (see, e.g., Fig. 6), approximately consists of three bands $E_m(\mathbf{k})$, one with each m character, and extending in a *double zone* of the *sparse* reciprocal sublattice spanned by

$$(\mathbf{a}^*, \mathbf{c}^* + \mathbf{b}^*, \mathbf{c}^* - \mathbf{b}^*). \quad (19)$$

This is the reciprocal of the *undimerized* lattice spanned by

$$\left(\mathbf{a}, \frac{\mathbf{c} + \mathbf{b}}{2}, \frac{\mathbf{c} - \mathbf{b}}{2}\right) = (\mathbf{a}, \mathbf{y} + \mathbf{z}, \mathbf{x} + \mathbf{z}), \quad (20)$$

with only *one* $\text{LiMo}_6\text{O}_{17}$ unit per primitive cell. The two last translations (20) we call *pseudo* translations. If expression (17) were true, the $E_m(\mathbf{k})$ band would be equivalent to the one translated by (any odd number of times) $-\mathbf{c}^*$, e.g., with $E_m(\mathbf{k} + \mathbf{c}^*)$, but the presence of the inversion and displacement dimerizations, (18) and (16), cause these two bands to gap where they cross, i.e., at the boundaries of the small zones. The resulting band structure is periodic in the proper (small) zone, corresponding to the proper primitive cell with *two* $\text{LiMo}_6\text{O}_{17}$ units, and has six continuous bands, two for each m , of which the lower is approximately $E_m(\mathbf{k})$ and the higher is approximately $E_m(\mathbf{k} + \mathbf{c}^*)$ in the odd-numbered zones; and

¹⁴We use a notation according to which a function, e.g., $\phi_R(\mathbf{r})$, $w(\mathbf{r}) \equiv w_{\text{Mo1}}(\mathbf{r})$, or $W(\mathbf{r}) \equiv W_{\text{MO1}}(\mathbf{r})$, of the space vector \mathbf{r} is centered at $\mathbf{r} = \mathbf{R} \equiv \mathbf{R}_R$, whereas a function such as $\phi_R(r)Y_{lm}(\hat{\mathbf{r}})$ of $r \equiv |\mathbf{r}|$ and $\hat{\mathbf{r}} \equiv \mathbf{r}/|\mathbf{r}|$ is centered at the origin.

the other way around in the even-numbered zones. As we shall see in paper II [1], ARPES approximately sees only the $E_m(\mathbf{k})$ -like band, i.e., both bands but separated in zones, and this will allow us to resolve the splitting and the perpendicular dispersion of the two quasi-1D bands in the gap.

The *undimerized* lattice has *one* $\text{LiMo}_6\text{O}_{17}$ unit per primitive cell and is spanned by the primitive translations (20) where, on the right-hand side, we have used the approximate relation (13). This shows that the undimerized lattice is 2D and hexagonal in the planes perpendicular to \mathbf{a} . This is the structure of the purple bronzes isolectronic with LiPB, $\text{NaMo}_6\text{O}_{17}$ and KM_6O_{17} , where CDW fluctuations with wave vector \mathbf{c}^* have been observed below 120 K and have been explained as driven by the simultaneous gapping of the 1D xz and the yz Fermi-surface (FS) sheets by one and the same nesting vector \mathbf{c}^* [32,68]. The lattice reciprocal to the undimerized one is spanned by (19), and its BZ is the double zone of the dimerized structure, i.e., that of LiPB shown in Fig. 8. Hence, we may consider the structure of quasi-1D LiPB as the CDW dimerization of quasi-2D Na or KPB, whose electronic structure consists of the 1D xy , yz , and xz bands dispersing at 120° relative to each other in the plane perpendicular to \mathbf{a} . The reason why the xy FS sheets do not also gap away is that relation (17) holds much better for the xy WOs than for the xz and yz WOs.

For comparison with Charts (14) and (15), the undimerized slab is

$$\begin{array}{c} \mathbf{c} \nearrow \\ \mathbf{a} \searrow \\ \mathbf{z} \uparrow \end{array} \begin{array}{cccccc} 4 & 1 & 2 & & 5 & 4 & 1 & 2 \\ 1 & 2 & & & 5 & 4 & 1 & 2 \\ 4 & & & & 5 & 4 & 1 & 2 \\ & & & & 5 & 4 & 1 & 2 & 5 \\ 5 & 4 & 1 & 2 & & & & & 5 & 4 & 1 \\ 4 & 1 & 2 & & 5 & 4 & 1 & 2 \end{array}, \quad (21)$$

where the steps of the staircase are smoothed out to a ramp, and the two ribbons are identical:

$$\begin{array}{c} \mathbf{b} \uparrow \\ \mathbf{c} + \mathbf{a} \rightarrow \\ \mathbf{y} \nearrow \\ \mathbf{x} \searrow \end{array} \begin{array}{cc} \text{Mo :} & \text{MO :} \\ \begin{array}{|c|c|} \hline 4 & 2 \\ \hline 5 & 1 \\ \hline 4 & 2 \\ \hline 5 & 1 \\ \hline 4 & 2 \\ \hline 5 & 1 \\ \hline \end{array} & \begin{array}{|c|c|} \hline 5 & 1 \\ \hline 4 & 2 \\ \hline 5 & 1 \\ \hline 4 & 2 \\ \hline 5 & 1 \\ \hline 4 & 2 \\ \hline \end{array} \end{array} \quad (22)$$

B. b dimerization

An unrelated and different dimerization is the one known from the description of the 1D band structure as two approximately 4-eV-broad, $1/4$ -filled xy bands [Fig. 3 and Eqs. (23) and (24)] running on zigzag chains along \mathbf{b} [26,27] and with the nearest-neighbor Mo1-Mo4 hopping integral $t \approx -1$ eV. In this view, Mo1 and Mo4 are inequivalent because of a dimerization from $\mathbf{b}/2$ to \mathbf{b} . In reciprocal space, this dimerization is from $2\mathbf{b}^*$ to \mathbf{b}^* and causes gaps at $k_b = \pm \frac{1}{2} \approx \pm 2k_F$, which separate the broad xy bands into two lower half-filled and two higher empty bands. The two latter bands will *not* be described by our set of six WOs, which are essentially Mo1-

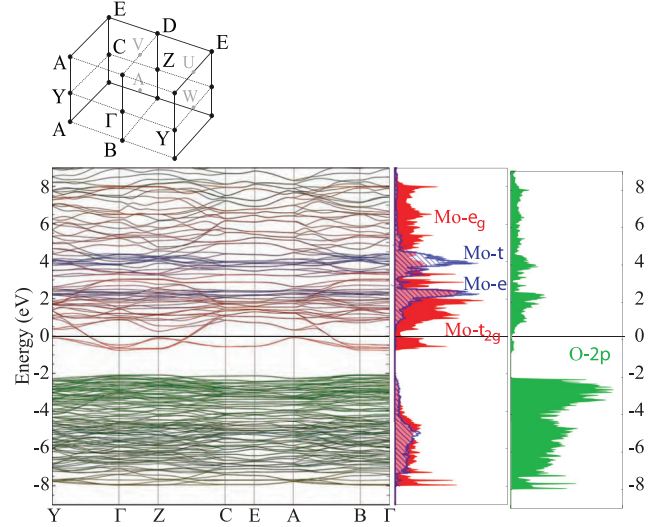


FIG. 3. The top shows half ($k_c \geq 0$) the (first) Brillouin-zone of $\text{LiMo}_6\text{O}_{17}$ with the labeling of the symmetry points for $P2_1/m$ obtained from the Bilbao crystal server [69]. The most relevant symmetry points have $k_a = 0$ and are $(k_b, k_c) = \Gamma(0, 0)$, $Y(\frac{1}{2}, 0)$, $W(\frac{1}{2}, \frac{1}{4})$, $C(\frac{1}{2}, \frac{1}{2})$, $Z(0, \frac{1}{2})$, $\Lambda(0, \frac{1}{4})$, and their equivalents. Below is the LDA band structure calculated with the large basis set of 336 NMTOs (left) and its partial densities of states (right) over a wide energy range. The zero of energy is the Fermi level of the stoichiometric compound.

Mo4 bonding orbitals (Fig. 9) but would require the inclusion of also Mo1-Mo4 antibonding orbitals, thus leading to a basis set unpractically large for our purpose of understanding the photoemission from the occupied bands.

IV. BASIC ELECTRONIC STRUCTURE

Shortly after the structural determination, Whangbo and Canadell [26] used the extended Hückel method to calculate and explain the basic electronic structure, but it took almost twenty years before a charge-self-consistent calculation could be performed. This was done by Popović and Satpathy [27] who used the LDA-DFT and the LMTO method. In the following, we explain and expand on these works using the insights gained from the view of the structure given in the previous section and from the results of the WO calculations to be presented in Secs. V and VI.

In Fig. 3, we show the LDA energy bands over a range of ± 9 eV around the Fermi level, together with their density of states projected onto O (green) and onto tetrahedrally- (blue) and octahedrally- (red) coordinated Mo. The bands between -8 and -2 eV have predominantly O $2p$ character and those extending upwards from $B \approx -0.7$ eV predominantly Mo $4d$ character and, above $+0.8$ eV, also Mo $5s$ and $5p$ character. The states in the O $2p$ band are bonding linear combinations with Mo $5s$, $5p$, and $4d$ orbitals, the more bonding, the lower their energy. The states in the Mo $4d$ band are antibonding linear combinations with O $2s$ and $2p$ orbitals; the more antibonding, the higher their energy.

The 2 eV gap between the O $2p$ -like and Mo $4d$ -like bands is – for the purpose of counting – ionic with Li donating one and Mo six electrons to and O acquiring two electrons

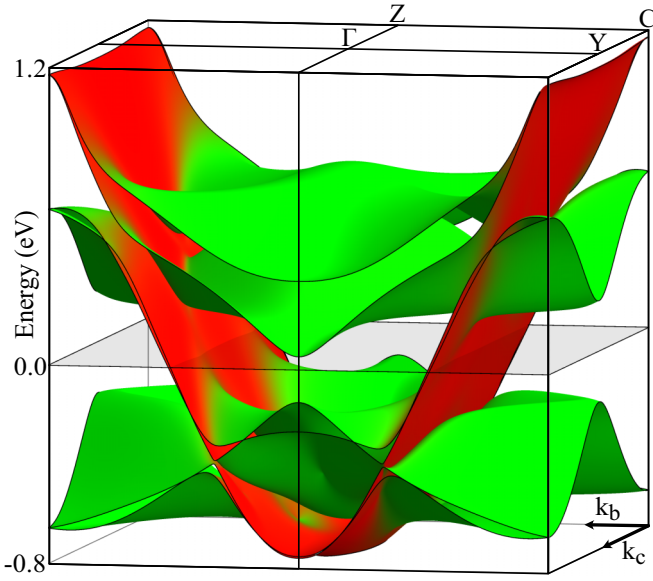


FIG. 4. LDA t_{2g} energy-band structure and Fermi level of LiPB at half filling. Red and green colors indicate, respectively, xy and xz or yz characters. The energy region is from 0.8 eV below to 1.2 eV above E_F (see Fig. 3) and the \mathbf{k} -space region is the BZ (see Fig. 8). The LDA TB parameters listed in Eqs. (43)–(47) were used, like in Fig. 12(a) in paper II [1].

from the Mo $4d$ -like bands above the gap, which thereby hold $2(1 + 6 \times 6 - 17 \times 2) = 6$ electrons per $2(\text{LiMo}_6\text{O}_{17})$. Had this charge been spread uniformly over all molybdenums, this would correspond to a Mo $d^{0.5}$ occupation.

The $4d$ orbitals forming the most antibonding and bonding states with O are the e_g orbitals, $3z^2 - 1$ and $x^2 - y^2$, on the octahedrally coordinated Mo because their lobes point toward the two O neighbors along z and the four O neighbors in the xy plane, respectively, and thereby form $pd\sigma$ bonds and antibonds. Not only the e_g orbitals on the octahedrally coordinated Mo, but all $4d$ orbitals (t and e) on the tetrahedrally coordinated Mo form filled bonding and empty antibonding states with their O neighbors, and thereby contribute to the stability of the crystal. However, as seen from the projected densities of states in Fig. 3, none of them contribute to the LDA bands within an eV around the Fermi level, which are those of our primary interest. So as long as there are no additional perturbations or correlations with energies in excess of this, which is assumed in the half-filled models, the Mo t and e orbitals are uninteresting for the low-energy electronics, and so are the Li $2s$ orbitals which contribute two bands several eV above the Fermi level, mix a bit with the oxygen states several eV below E_F , and donate their two electrons to them. Due to the Pauli principle, changing the Li content (doping) will change the position of the Fermi level, which is inside the Mo t_{2g} bands.

Although the MoO_4 tetrahedra do not contribute any electrons near the Fermi level, their arrangement in double layers perpendicular to \mathbf{a} , separating the staircases of corner-sharing octahedra, has an important impact on the low-energy electronic structure: It suppresses the hopping between the

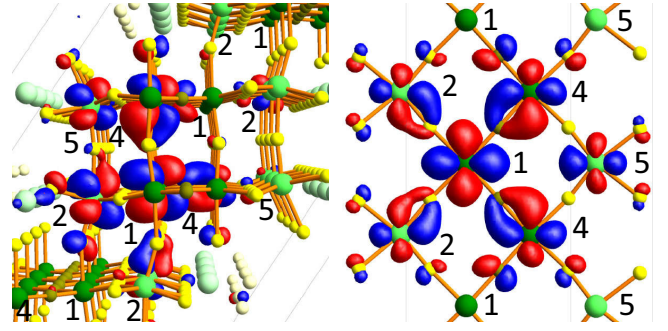


FIG. 5. (Left) yz standing-wave state with $k_c + k_b = \pm 1/2$ which behaves like $\cos 2\pi \frac{1}{2}(r_c + r_b)$. View along \mathbf{b} as in Fig. 2(c) and Charts (14) and (33). (Right) xy standing-wave state with $|k_b| = 1/4 \sim k_F$ which behaves like $\cos 2\pi \frac{1}{4}r_b$. View along $-\mathbf{z} \sim \mathbf{a} - \mathbf{c}$ as in Fig. 2(d) and Charts (15) and (34). The sign of a lobe is indicated by its color. See also Fig. 9 with caption. As explained in Sec. VI, these figures are identical with those shown in Fig. 9 of the yz and xy Wannier orbitals (WOs) on site 1. The xy WO has a halo consisting of xy partial waves on the four nearest Mo neighbor sites, 4 and 2, plus a weaker one on the next-nearest Mo-neighbor site 5. The yz WO has a halo consisting of yz partial waves (of unequal magnitude) on the two nearest Mo neighbor sites 4, plus weaker ones on Mo2 and 5.

low-energy orbitals across the double layer to the extent that we shall neglect it in our TB model for the six lowest bands.¹⁵

A. The t_{2g} bands

The remaining $4d$ orbitals on octahedrally coordinated Mo are the t_{2g} orbitals, xy , xz , and yz , whose lobes point *between* the four O neighbors in, respectively, the xy , xz , and yz planes and therefore form relatively weak $pd\pi$ bonds and antibonds, e.g., Mo $xy \pm O_y$ on the $\mathbf{x}/2$ bond. Whereas the bonds are dominated by oxygen and form bands that are part of the O $2p$ continuum below about -4 eV, the *antibonds* are dominated by Mo and form $4 \times 2 \times 3 = 24$ bands which extend from $+3.0$ eV down to the bottom of the Mo $4d$ continuum at -0.7 eV. This spread in energy is *conventionally* described as due to hopping between *dressed* Mo t_{2g} orbitals, where the dressing consists of the $pd\pi$ antibonding tails on the four oxygens in the plane of the orbital. Since the dressed orbitals are planar, the strongest hoppings are between *like* t_{2g} orbitals which are nearest neighbors in the same plane, e.g., as seen in the right-hand panel of Fig. 5 between the dressed xy orbital on Mo1_o and those on Mo4_x, Mo4_y, Mo2_{-x}, and Mo2_{-y}, or as seen in the left-hand panel between the dressed yz orbital on

¹⁵As seen in Fig. 2(b) and Chart (14), the shortest path for hopping of low-energy electrons across the double layer of tetrahedrally coordinated molybdenums is Mo5 - (MO6) - MO5, i.e., from Mo5 in a bottom ribbon, along $-\mathbf{z}$ to (MO6) in the top ribbon of the neighboring staircase, and then along $-\mathbf{x}$ or $+\mathbf{y}$ to MO5 in that top ribbon. This zigzag path thus passes via merely *one* tetrahedrally coordinated Mo atom and gives rise to the slight k_a dispersion of the two nearly degenerate xy bands seen most clearly in Fig. 3 along CE and 1 eV above the Fermi level.

Mo1_o and those on Mo4_y, Mo4_z, Mo2_{-y}, and Mo2_{-z}. These hoppings are $dd\pi$ -like and of magnitude $t = -1$ eV.

The main dispersion of the xy band is, therefore, in the direction of the xy lobe pointing along $\mathbf{y} - \mathbf{x} = \mathbf{b}$, that of the yz band is in the direction of the yz lobe pointing along $\mathbf{y} + \mathbf{z} = \frac{\mathbf{c} + \mathbf{b}}{2}$ (see left panel of Fig. 5), and that of the xz band is in the direction of the xz lobe pointing along the $\mathbf{x} + \mathbf{z} = \frac{\mathbf{c} - \mathbf{b}}{2}$; see Charts (14) and (15).

1. The four xy bands

The right-hand panel of Fig. 5 shows the xy standing-wave state with $|k_b| = \frac{1}{4} \sim k_F$ which behaves like $\cos 2\pi k_b \mathbf{b}^* \cdot \mathbf{b} r_b \equiv \cos 2\pi \frac{1}{4} r_b$, i.e., is even around the $\mathbf{c} + \mathbf{a}$ line through Mo1 and Mo5 and has nodes at the Mo1-Mo5 lines translated by $\pm \mathbf{b}$. Here, the orientation is like in Fig. 2(d) with the Mo numbering given in the left-hand panel of Chart (15). We see that the amplitudes of the dressed xy orbitals are largest at Mo1 and decrease in the order Mo4, Mo2, and Mo5, thus following the decrease of the Mo coordination mentioned in Sec. III A. The dressed orbitals on the four nearest neighbors (Mo4 at x and y , and Mo2 at $-x$ and $-y$) antibond to the central orbital, i.e., nearest-neighbor lobes have different colors. This is the reason why the overlap from the neighboring dressed xy orbital weakens the O y (or x) amplitude on the common oxygen such that its contour merges with that of the weaker Mo neighbor. Hence, O p is $pd\pi$ antibonding with Mo1 xy and bonding with Mo4 xy and Mo2 xy . The net result is $pd\pi$ nonbonding, essentially.

The xy band disperses almost exclusively in the \mathbf{b} direction, and now, we imagine going to the xy state with $|k_b| = \frac{3}{4} = \frac{1}{4} [\text{mod } \frac{1}{2}]$ and energy ≈ 2.8 eV above E_F , i.e., to the state in the *next* xy band. Here, the signs (colors) of the dressed xy orbitals on the four nearest neighbors (Mo4 and Mo2) will have changed, whereby the overlaps on the common oxygens shared with Mo1 will have their amplitudes enhanced and the O y (or x) contour will be separated by a node, not only from the stronger Mo1- xy contour, but also from the weaker Mo4- xy (or Mo2- xy) contour. In the following, we refer to the xy band with the lower (higher) energy as the Mo1-Mo4 bonding (antibonding) band, although both of these bands are $pd\pi$ non- or antibonding; but the one with the lower energy has fewer $pd\pi$ nodes.

The dressed xy orbitals lie in the plane of a ribbon, and those along the infinite zigzag chain, $\overset{\mathbf{x}}{\rightarrow} \text{Mo1} \overset{\mathbf{y}}{\rightarrow} \text{Mo4} \overset{\mathbf{x}}{\rightarrow}$, with *pseudo* translation $(\mathbf{y} - \mathbf{x})/2 = \mathbf{b}/2$ form the well-known [19,26,27] quasi-1D band with dispersion:¹⁶

$$\varepsilon_{xy}(\mathbf{k}) \sim 2t \cos \left(2\pi \mathbf{k} \cdot \frac{\mathbf{b}}{2} \right) = 2t \cos \pi k_b, \quad (23)$$

where $t \approx -1$ eV. Since \mathbf{b} , and not $\mathbf{b}/2$, is the proper lattice translation because Mo1 and Mo4 are not equivalent, the band must be folded from the large BZ bound by the midplanes ($k_b = \pm 1$) of the reciprocal-lattice vectors $\pm 2\mathbf{b}^*$, into the proper, small BZ bound by the midplanes ($k_b = \pm \frac{1}{2}$) of $\pm \mathbf{b}^*$ whereby it becomes $-2t \cos \pi k_b$. An equivalent

prescription—more useful than BZ folding, as we shall see below for the bonding yz and xz bands,—is to say that if \mathbf{k} must be limited to the proper, small BZ, then we must also consider the band

$$\varepsilon_{xy}(\mathbf{k} + \mathbf{b}^*) \sim 2t \cos [\pi(k_b + 1)] = -2t \cos \pi k_b, \quad (24)$$

translated by the proper reciprocal-lattice vector $-\mathbf{b}^*$. Finally, the *inequivalence* of—or “dimerization into”—Mo1 and Mo4 couples the $xy(\mathbf{k})$ and $xy(\mathbf{k} + \mathbf{b}^*)$ bands, and where they are degenerate—which is for $|k_b| = 1/2$, i.e., at the boundaries of the proper BZ (YC)—they are gapped by ± 0.3 eV. Since this gap is relatively large, the $xy(\mathbf{k})$ band is bonding and the $xy(\mathbf{k} + \mathbf{b}^*)$ band antibonding between Mo1 and Mo4 for \mathbf{k} inside the proper BZ. The latter empty xy band, which extends from approximately 1.7 to 3.4 eV above E_F , we neglect in the bulk of the present papers, as was already mentioned in Sec. III B.

Degenerate and parallel with the Mo1-Mo4 bonding and antibonding xy bands running along the lower ribbon are MO4-MO1 bonding and antibonding XY bands running along the upper ribbon [see Fig. 2(d), Chart (14), and the right-hand panel of Chart (15)]. Their $|k_b| = 1/4 \sim k_F$ standing-wave state looks like the one shown on the right-hand side of Fig. 5, but has MO1 on top of Mo4 and vice versa. Viewed along \mathbf{b} , the appearance of the xy and XY states is like that of the xy and XY WOs in the first two columns on the top row of Fig. 9. From there, we realize that these flat, parallel states are well separated, each one on its own ribbon, with no contribution of the oxygens in between. The $dd\delta$ -like hops between the xy and XY orbitals inside the same bi-ribbon ($t_{\perp} \equiv t_1 + u_1 \approx -14$ meV) and between the XY and xy orbitals in different bi-ribbons ($t'_{\perp} \equiv t_1 - u_1 \approx -8$ meV), give the bands a *perpendicular* (k_c) dispersion, which is two orders of magnitude smaller than the k_b dispersion given by Eq. (23). If all ribbons were translationally equivalent, i.e., if the primitive translations (neglecting \mathbf{a}) were $\mathbf{x} + \mathbf{z} = (\mathbf{c} - \mathbf{b})/2$ and $\mathbf{y} + \mathbf{z} = (\mathbf{c} + \mathbf{b})/2$ with reciprocal-lattice translations $\mathbf{c}^* - \mathbf{b}^*$ and $\mathbf{c}^* + \mathbf{b}^*$, the $dd\delta$ hopping would add

$$2t_1 [\cos \pi(k_c - k_b) + \cos \pi(k_c + k_b)] = 4t_1 \cos \pi k_b \cos \pi k_c$$

to Eq. (23). But since the primitive translations are really \mathbf{b} and \mathbf{c} , we must—if we want to confine \mathbf{k} to the proper BZ—also add the equivalent term translated by the proper reciprocal-lattice vector,¹⁷ $-\mathbf{c}^*$. As a result, we get for the two half-filled xy bands:

$$\varepsilon_{xy} \left(\begin{array}{c} \mathbf{k} \\ \mathbf{k} + \mathbf{c}^* \end{array} \right) \sim 2t [1 \pm (2t_1/t) \cos \pi k_c] \cos \pi k_b, \quad (25)$$

where the distortion caused by the gap extending upwards from ≈ 1.1 eV above E_F has been neglected. As long as \mathbf{k} is inside the first BZ ($|k_c| \leq \frac{1}{2}$), the $xy(\mathbf{k})$ band is bonding and the $xy(\mathbf{k} + \mathbf{c}^*)$ band is antibonding between ribbons, i.e., between xy and XY . In the second BZ ($|k_c - 1| \leq 1/2$), the opposite is true (see Fig. 6). The translational *inequivalence* of the two ribbons—i.e., the dimerization into bi-ribbons—

¹⁶We denote energy bands $E(\mathbf{k}) = \varepsilon(\mathbf{k}) + E_0$ and their dispersions $\varepsilon(\mathbf{k})$. Here, E_0 is the center of the band.

¹⁷Substituting \mathbf{c}^* by $-\mathbf{c}^*$ gives the same result because their difference $2\mathbf{c}^*$ is a translation of the reciprocal lattice spanned by $\mathbf{c}^* - \mathbf{b}^*$ and $\mathbf{c}^* + \mathbf{b}^*$.

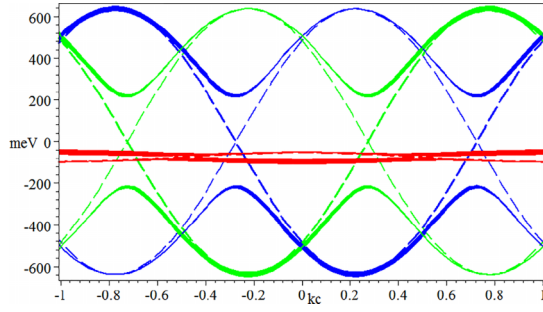


FIG. 6. The six pure- m t_{2g} bands ($m = yz$ green, xz blue, and xy red) as functions of k_c in the double zone ($-1 < k_c \leq 1$) and for $k_b = 0.225$, i.e., along the brown dot-dashed line containing P and Q in Fig. 8. 10% hole doping will place the Fermi level inside the red bands. The $m(\mathbf{k})$ and $m(\mathbf{k} + \mathbf{c}^*)$ bands, whose dispersions are described in Sec. IV A, have period $\Delta k_c = 2$ and are shown in, respectively, fat and normal dashed lines. The $\{m(\mathbf{k}), m(\mathbf{k} + \mathbf{c}^*)\}$ hybridized bands have period 1 and are shown in full lines. Their *additional* (vertical) fatness is proportional to the $|\mathbf{k}|$ character and has period 2. The ARPES-refined TB parameters listed in Eqs. (43), (44), (45), and (49) were used and, accordingly, the zero of energy is the center of the gap, i.e., the common energy of the xz , XZ , yz , and YZ WOs. The Fermi level of samples G and H is at $+75$ meV.

finally splits the degeneracy of the $xy(\mathbf{k})$ and $xy(\mathbf{k} + \mathbf{c}^*)$ bands at the BZ boundaries $|k_c| = 1/2$ (the ZCED planes) by $\pm 2\sqrt{2}u_1 \cos \pi k_b$, which for $k_b = 1/4 \sim k_F$ is a mere ± 8 meV.

2. The two yz and the two xz bands

In the planes perpendicular to the bi-ribbons [Fig. 2(c) and Chart (14)] and cutting them along the \mathbf{y} strings [Fig. 2(d) and Chart (15)] lie the dressed yz orbitals, and in the planes cutting along the \mathbf{x} strings lie the dressed xz orbitals. The left-hand panel of Fig. 5 shows that $|k_c + k_b| = 1/2$ standing-wave state of the yz band which behaves like $\cos 2\pi \frac{1}{2}(r_c + r_b)$, i.e., is even around the Mo1-containing planes which are perpendicular to $\mathbf{c}^* + \mathbf{b}^*$ and has nodes in the MO1-containing planes. Like for xy state in the right-hand panel of Fig. 5, the dressed yz orbitals on the four nearest neighbors in the plane of the orbital (MO4 at \mathbf{z} , Mo4 at \mathbf{y} , Mo2 at $-\mathbf{y}$, and Mo2 at $-\mathbf{z}$) are $dd\pi$ antibonding with the dressed yz on the central Mo1, which means $pd\pi$ nonbonding with the oxygen. Here again the amplitudes of the dressed yz orbitals decrease like the Mo coordination.

Whereas in the plane of the xy orbital, Mo4—like Mo1—has four nearest neighbors of molybdenums coordinated octahedrally with oxygen, in the plane of the yz orbital, Mo4 has only three neighbors, and so does Mo2, while Mo5 has merely two. As noted in Sec. III A, this is due to the stacking into a staircase of bi-ribbons (14). As a result, the yz orbitals on the Mo1- and MO1-sharing zigzag double chain,

$$\begin{array}{c} \mathbf{c} \\ \mathbf{a} \\ \mathbf{z} \end{array} \left\{ \begin{array}{ccccccc} & & 5 & \rightarrow 4 & \uparrow 1 & \rightarrow 2 \uparrow & \\ & & & \rightarrow 2 & \uparrow 1 & \rightarrow & \uparrow 4 & 5 \\ 5 & \rightarrow 4 & \uparrow 1 & \rightarrow & 2 \uparrow & & & \\ \rightarrow 2 & \uparrow 1 & \rightarrow & 4 \uparrow & & 5 & & \end{array} \right\}, \quad (26)$$

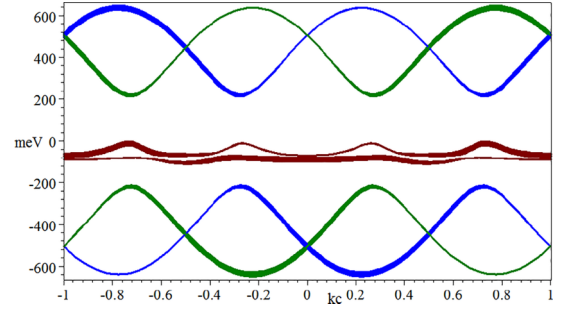


FIG. 7. Like Fig. 6 ($k_b = 0.225$) but including the hybridization of the \tilde{xy} band (dark red) with the xz (blue) and yz (green) valence and conduction bands via Löwdin downfolding as explained in paper III [2]. This hybridization brings in the parameters $\alpha_n \pm \gamma_n$ and $a_n \pm g_n$ [Eqs. (39) and (46)]. Not included in this figure are the xy hybridizations of the blue xz and the green yz bands, as well as the hybridization between the xz and yz bands.

running up the staircase with pseudotranslation $\mathbf{z} + \mathbf{y} = (\mathbf{c} + \mathbf{b})/2$, form a quasi-1D band dispersing like

$$\varepsilon_{yz}(\mathbf{k}) = 2A_1 \cos [2\pi \mathbf{k} \cdot (\mathbf{c} + \mathbf{b})/2] = 2A_1 \cos \pi(k_c + k_b), \quad (27)$$

with an effective hopping integral, $A_1 \approx -0.3$ eV and bandwidth $4|A_1| \approx 1.2$ eV. Because the hopping between ribbons proceeds via Mo4 inside the bi-ribbon, but via Mo2 between bi-ribbons and because the former distance is shorter than the latter, the hopping integrals are different, respectively $A_1 + G_1 \approx -0.3 - 0.1 \approx -0.4$ eV and $A_1 - G_1 \approx -0.2$ eV. This dimerization into bi-ribbons causes \mathbf{c} rather than $(\mathbf{c} + \mathbf{b})/2$ to be a primitive lattice translation whereby the $yz(\mathbf{k} + \mathbf{c}^*)$ band with dispersion

$$\varepsilon_{yz}(\mathbf{k} + \mathbf{c}^*) = -2A_1 \cos \pi(k_c + k_b) \quad (28)$$

is equivalent to the $yz(\mathbf{k})$ band (27). Where these bands are degenerate, i.e., for $|k_c + k_b| = 1/2$, they gap by $\pm 2|G_1| \approx \pm 0.2$ eV whereby they become

$$\varepsilon_{yz} = \pm \sqrt{[2A_1 \cos \pi(k_c + k_b)]^2 + [2G_1 \sin \pi(k_c + k_b)]^2}. \quad (29)$$

For \mathbf{k} between the $|k_c + k_b| = 1/2$ planes, the $yz(\mathbf{k})$ and $yz(\mathbf{k} + \mathbf{c}^*)$ bands are, respectively, bonding and antibonding between neighboring ribbons. The two yz bands, decorated by the \mathbf{k} character (27), are shown in green in Fig. 6.

It should be noted that the gapping takes place for $|k_c + k_b| = 1/2$, which is *not* at the boundary of the conventional BZ, $|k_b| = 1/2$ and $|k_c| = 1/2$ shown in Figs. 3 and 8, but where the $\varepsilon_{yz}(\mathbf{k})$ and $\varepsilon_{yz}(\mathbf{k} + \mathbf{c}^*)$ bands are degenerate. Nevertheless, the zone centered at $\Gamma(0, 0)$ and bound by the planes $|k_b| = 1/2$ and $|k_c + k_b| = 1/2$ (ZYAD) is a primitive cell of the reciprocal lattice, and we call it a *physical zone*, useful for understanding properties of the yz bands.

With the substitution: $\mathbf{b} \rightarrow -\mathbf{b}$, everything said about the yz bands holds for the xz bands (shown in blue in Fig. 6).

As regards choices of zones, we can either take

$$|k_b| \leq \frac{1}{2} \text{ and } |k_c| \leq \frac{1}{2}, \quad (30)$$

$$|k_b| \leq \frac{1}{2} \text{ and } |k_c + k_b| \leq \frac{1}{2}, \quad (31)$$

$$\text{or } |k_b| \leq \frac{1}{2} \text{ and } |k_c - k_b| \leq \frac{1}{2}, \quad (32)$$

but *not* $|k_c + k_b| \leq 1/2$ and $|k_c - k_b| \leq 1/2$ whose volume (area) is only *half* the BZ volume (see Fig. 8). Expressions (30)–(32) thus define the *physical zones* for, respectively, the xy , yz , and xz bands.

3. Lineup of the six lowest t_{2g} bands

The bottoms of the xz and yz bands and those of the degenerate xy bands are *all* at $\Gamma(\mathbf{k} = \mathbf{0})$ and at the energy of that linear combination of the dressed xz , yz , or xy orbitals which is the least antibonding between all octahedral molybdenums (Fig. 3). According to the LDA, these energies are $B_{xz/yz} \sim E_F - 0.6$ eV and $B_{xy} \sim E_F - 0.7$ eV. Since the $4|A_1|$ width of the xz and yz bands is only about one third the $4|t|$ width of the xy bands, the $4|G_1|$ gap halfway up in the xz and yz bands extends between the energies $B_{xz/yz} + 2|A_1 \pm G_1| \approx \pm 0.2$ eV with respect to the Fermi level set by the half-filled, lower xy bands. In the following paper II [1] (see, e.g., Fig. 12 of paper II), we see that agreement with ARPES requires a 0.1 eV downward shift of the xz or yz bands with respect to the xy bands, whereby $B_{xz/yz} \sim E_F - 0.7$ eV $\sim B_{xy} \equiv B$. This low-energy t_{2g} band structure is shown in Fig. 6 along the line $k_b = 0.225$ perpendicular to \mathbf{b} , the direction of quasi 1D conductivity.

In summary, since the six lowest bands are t_{2g} -like, the six electrons would half fill them in case of weak Coulomb correlations, thus corresponding to a t_{2g}^3 configuration. Covalency between the xz and XZ orbitals, as well as between the yz and YZ orbitals, together with the availability of one xz and one yz electron per string, result in the covalent bonds which dimerize the ribbons into bi-ribbons and thereby gap the xz and yz bands into filled bonding and empty antibonding bands. The remaining one xy electron per string finally half fills the quasi-1D band dispersing strongly along \mathbf{b} .

The six t_{2g} bands are illustrated in Fig. 4, from where it is seen that the gaps in the green xz and yz bands are around the center of the red, metallic xy bands and, hence, around the gray, transparent Fermi level.

4. Constant-energy contours

Figure 8 shows the double zone, $|k_b| \leq 1/2$ and $|k_c| \leq 1$, and—schematically and in weak lines—the constant-energy contours (CECs) for the $xz(\mathbf{k})$ bands in blue, the $yz(\mathbf{k})$ bands in green, and the (almost) degenerate, half-filled $xy(\mathbf{k})$ and $xy(\mathbf{k} + \mathbf{c}^*)$ bands (25) in red. The bottoms of these four bands are along, respectively the blue, green, and red lines passing through $\Gamma(0, 0)$. The tops of the $xz(\mathbf{k})$ and $yz(\mathbf{k})$ bands are along the blue and green lines passing through $\Gamma'(0, \pm 1)$. The top of the degenerate xy bands [which is a cusp because Eq. (25) neglects the Mo1–Mo4 gap] is along the red, vertical BZ boundary $|k_b| = 1/2$.

For the degenerate xy bands, we also show the CECs for three energies close to the Fermi level corresponding to half filling (red dot-dashed), 10% hole (brown dot-dashed), and 10% electron (olive dot-dashed) doping. For the gapped $xz(\mathbf{k})$ and $xz(\mathbf{k} + \mathbf{c}^*)$ bands we show the coinciding CECs for the valence- and conduction-band edges (blue solid lines), and similarly for the yz -band edges (green solid lines). The CECs for the $xz(\mathbf{k} + \mathbf{c}^*)$ and $yz(\mathbf{k} + \mathbf{c}^*)$ bands of course equal those

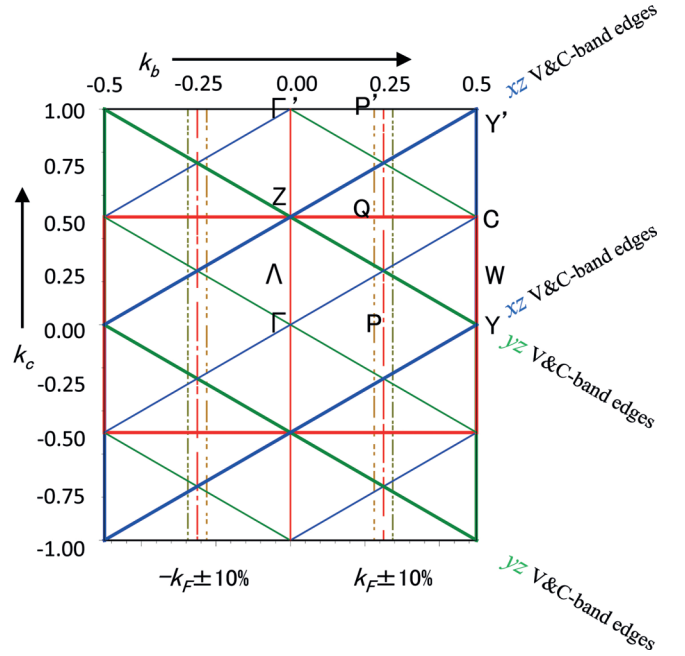


FIG. 8. Double zone: $-0.5 < k_b \leq 0.5$ and $-1 < k_c \leq 1$. The red, blue, and green solid lines show the *physical zones* for, respectively the xy , xz , and yz pure bands; see Eq. (30), (32), and (31). The red zone is the BZ, and its irreducible part is the one with $0 \leq k_c \leq 0.5$. The reciprocal-lattice points are $\mathbf{G} = M\mathbf{b}^* + N\mathbf{c}^*$, i.e., $(k_b, k_c) = (M, N)$, with M and N integers. Those (19) with $M + N$ even, form the lattice reciprocal of the un-dimerized lattice (20) whose BZ is the double zone. Shifting this even reciprocal lattice by \mathbf{c}^* yields the *odd* reciprocal lattice; see Sec. VIB. Weak lines indicate the positions of pure-band maxima and minima (see Fig. 6). The red dot-dashed lines indicate the positions of the left and the right, doubly degenerate Fermi-surface sheets for stoichiometric $2(\text{LiMo}_6\text{O}_{17})$. The brown and olive dot-dashed lines correspond to 10%, respectively, hole and electron doping. Because $c/b = 1.720 \approx \sqrt{3}$, the $\Gamma\Gamma'$ triangles are almost equilateral, and since this is so in the present figure, it is to scale. The k_b axis, has been turned by $\approx 90^\circ$ with respect to \mathbf{b} in the real-space Figs. 2(d), and 5 (right).

for, respectively, the $xz(\mathbf{k})$ and $yz(\mathbf{k})$ bands but translated along k_c by an odd integer.

As seen in Fig. 7 for $k_b = 0.225$, corresponding to 10% hole doping, the xz and yz valence-band edges running along $|k_c \mp k_b| = 1/2$ (YZY') and merely 0.2 eV below the xy bands push *resonance peaks* up at $|k_c| = 0.725$ and 0.275 in the upper xy band. This gives rise to “notches” pointing towards Z (Fig. 8) in the inner sheets of xy CECs with energies in the lower half of the gap. Near $k_c = 0$ (ΓY) and $k_c = \pm 1$ ($\Gamma' Y'$), hybridization with the xz and yz valence and conduction bands, which are now 0.5 eV away (Fig. 7), reduces the $dd\delta$ -like splitting (25) between the xy bands seen Fig. 6 to become almost a *contact* between the two xy bands and CECs. Near the BZ boundaries, $|k_c| = 1/2$ (ΓC), mixing of the $xy(\mathbf{k})$ and $xy(\mathbf{k} + \mathbf{c}^*)$ bands and hybridization of the lower with the xz and yz conduction bands 0.5 eV above, pushes down *bulges* in the lower xy band, thus causing the outer CEC sheets to bulge outwards. We shall search for these features using new ARPES measurements in paper III [2], devoted to the detailed

study and explanation of the splitting and perpendicular dispersion of the quasi-1D metallic bands in the gap.

V. LOW-ENERGY WANNIER ORBITALS

In the previous section, our view moved from the energy scale of the Li $2s$, Mo $5sp$, $4d$, and O $2p$ atomic shells to the decreasing energy scales of the Li^+ , Mo^{6+} , and O^{2-} ions, to the covalently bonded MoO_4 tetrahedra and MoO_6 octahedra and, finally, to the low-energy bands of the MoO_6 octahedra condensed into strings, ribbons, and staircases of bi-ribbons by sharing of the $pd\pi$ -bonded O corners. In this change of focus from large to small energy scales and, concomitantly, from small to large spatial scales, we have followed computationally with the NMTO method in the LDA by using increasingly narrow and fine energy meshes and increasingly sparse basis sets as was described in Sec. II.

The *six lowest Mo 4d bands*, i.e., those within ± 0.75 eV around the Fermi level (see Figs. 3 and 4) were found to be completely described by the basis set consisting of the three xy , xz , and yz NMTOs centered on Mo1 plus the three equivalent ones (18) centered on MO1, that is, of *one t_{2g} set per string*, which is per $\text{LiMo}_6\text{O}_{17}$. Symmetrical orthonormalization yielded the corresponding set of WOs whose xy and yz orbitals are what was actually shown in Fig. 5. The centers of the t_{2g} WOs were chosen at Mo1 and MO1 because those are the only octahedral molybdenums whose six nearest molybdenum neighbors are also octahedrally surrounded by O.

Each WO spreads out to the four nearest octahedral molybdenums in the plane of the orbital and, as explained in the previous sections, this leads to almost half the WO charge being on Mo1, slightly less on Mo4, considerably less on Mo2, and much less on Mo5. There is no discrepancy between the t_{2g}^3 configuration and the Mo $d^{0.5}$ occupancy mentioned at the beginning of Sec. IV: The latter is an average over all six molybdenums in a string of which only four carry t_{2g} partial waves, which are combined into *one* set of t_{2g} WOs, each one being effectively spread onto three molybdenums. So the occupation is perhaps more like Mo d^1 .

What *localizes* a $t_{2g,m}$ WO in the set of all three t_{2g} WOs on all Mo1 and MO1 atoms, is the condition that its projections onto all t_{2g} partial waves on all Mo1 and MO1 atoms, *except* the $t_{2g,m}$ partial wave on the own site, must *vanish*.¹⁸ On the other hand, the WO spreads onto any *other* site and partial wave in the crystal in such a way that the WO set spans the solutions of Schrödinger's equation at the $N + 1 = 3$ chosen energies. For the view (14), this is schematically

$$\begin{array}{l}
 \mathbf{c} \nearrow \\
 \mathbf{a} \searrow \\
 \mathbf{z} \uparrow
 \end{array}
 \begin{array}{|c|c|c|c|}
 \hline
 4 & 5 & 2 & \circ & 4 \\
 & 5 & 4 & \circ & 2 \\
 & 2 & \bullet & 4 & 5 \\
 \hline
 5 & 4 & \circ & 2 & 5 \\
 2 & \circ & 4 & 5 & 2
 \end{array}, \quad (33)$$

¹⁸Strictly speaking, this holds for the set of KPWs rather than of NMTOs and of WOs (see Sec. II).

with \bullet indicating the site (here Mo1) of the WO, and \circ the sites where all t_{2g} characters are required to vanish, i.e., the sites of the other WOs in the t_{2g} set. For the view (15), the Mo1-centered WO is

$$\begin{array}{l}
 \mathbf{b} \uparrow \\
 \mathbf{c} + \mathbf{a} \rightarrow \\
 \mathbf{x} \searrow \\
 \mathbf{y} \nearrow
 \end{array}
 \begin{array}{|c|c|c|}
 \hline
 \text{Mo :} & & \\
 \hline
 \circ & 5 & \\
 2 & 4 & \\
 \bullet & 5 & \\
 2 & 4 & \\
 \circ & 5 & \\
 \hline
 \end{array}
 \begin{array}{|c|c|}
 \hline
 \text{MO :} & \\
 \hline
 4 & 2 \\
 5 & \circ \\
 4 & 2 \\
 5 & \circ \\
 4 & 2 \\
 \hline
 \end{array}. \quad (34)$$

Our t_{2g} WOs are insensitive to the exact orientation chosen for the xyz system—we took the one given by Eq. (12)—because they have all partial waves *other than* xy , xz , and yz on Mo1 and MO1 downfolded.¹⁹ The contents of these partial waves are thus determined uniquely by the requirement that the WO basis set solves Schrödinger's equation exactly at the chosen energies for the LDA potential used to construct the WOs. In this way, the downfolding procedure ensures that the shape of t_{2g} orbitals is given by the *chemistry* rather than by the choice of directions. Specifically, the downfolded content of partial waves with e_g character rotates the directions of the t_{2g} lobes into the proper “chemical” directions [42]. Moreover, the downfolded partial-wave contents on the remaining Mo2, Mo4, and Mo5 atoms in the string ensure that their relative phases are the proper ones for the energies chosen. Also, a WO on the upper string is correctly inverted with respect to the one on the lower string [see Eq. (18)]. Similarly, the downfolded partial waves on all oxygens give the proper O $2p$ dressing.

The WOs are obtained by symmetrical orthonormalization of the NMTO set and this causes a delocalization which, however, for our t_{2g} set is small and invisible in Fig. 5. What we do see and is noted in the previous section is that each t_{2g} WO has tails with the same t_{2g} character as that of the head on the four nearest molybdenums in the plane of the orbital. These tails are connected to the head via $pd\pi$ tails on the four connecting oxygens such that the sign is antibonding with the t_{2g} head and bonding with the t_{2g} tail. In effect, this results in a $dd\pi$ antibond between the oxygen-dressed t_{2g} orbitals forming the WO head and tail.

Since the xy WO lies *in* the plane of its ribbon, it only spreads onto a neighboring ribbon via a weak covalent interaction of symmetry $dd\delta$ causing no visible tails in the upper rows of Fig. 9. This is in contrast with the strong inter-ribbon $dd\pi$ spread of the xz and yz WOs. The consequence for the six-band Hamiltonian to be presented in the next section is that the xy - XY inter-ribbon hopping integral t_1 in Eq. (25) and its dimerization u_1 are about 30 times smaller than the respective xz - XZ and yz - YZ inter-ribbon integrals A_1 and G_1

¹⁹For the XYZ system located on MO1 in the upper ribbon, we merely translate the xyz system from Mo1 to MO1. These two parallel, local coordinate systems do *not* follow the space-group symmetry, specifically the center of inversion between the nearest Mo1-MO1 neighbors. But the t_{2g} projections on the Mo1 and MO1 hard spheres do, because they are even, and this is all that matters for the WOs.

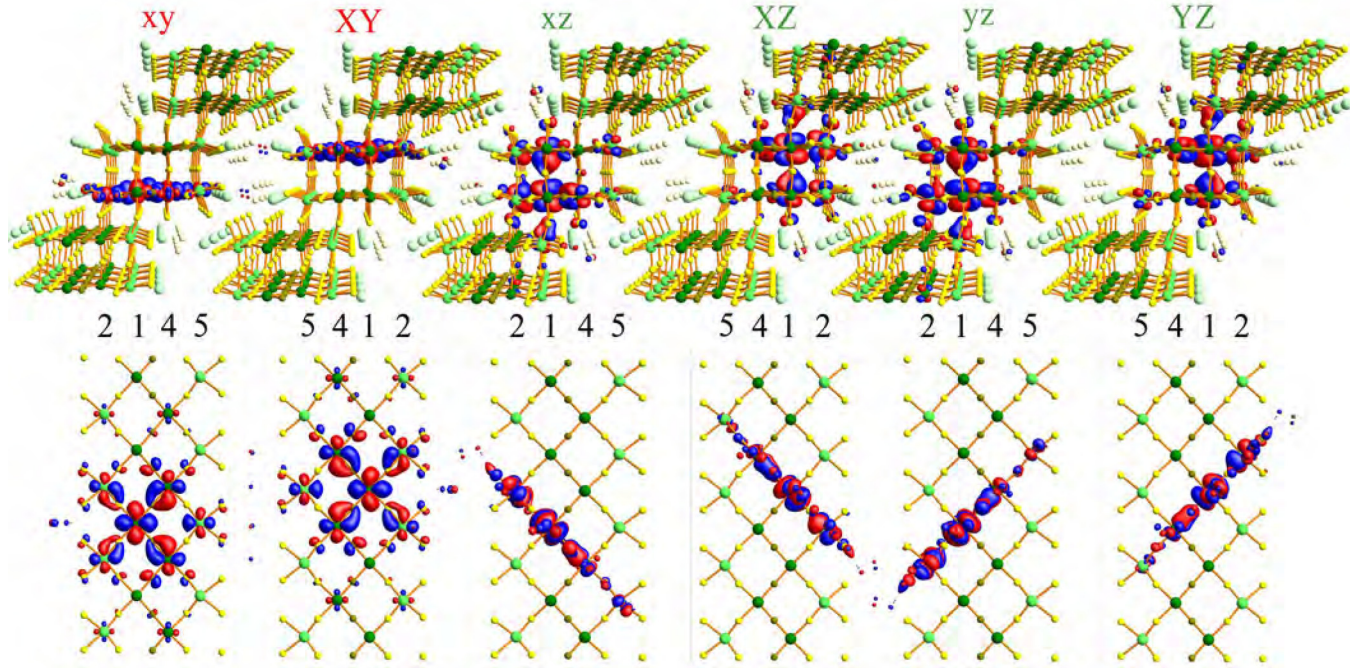


FIG. 9. The six Mo1- and MO1-centered t_{2g} WOs spanning the six lowest energy bands of $2(\text{LiMo}_6\text{O}_{17})$ shown in Fig. 4. The orientation is as in Fig. 2(c) and 2(d), with the numbering of the octahedrally coordinated molybdenums given in, respectively, Charts (14) and (15). Shown are the WO's constant-density surfaces containing 70% of the WO's charge with the color giving the sign of the lobe. With the usual 90% cutoff, as e.g., used for the t_{2g} WOs in NiO [52]), the overlaps would have been obscurely large. This more diffuse character of the LiPB WOs is needed in order that they accurately describe bands that are not visibly separated from the higher, more antibonding bands [see Fig. 3, and the long-range of the hopping integrals in (43), (46), and (47)]. The slices shown in Fig. 5 of standing-wave yz and xy states equal the corresponding WO, because for the values of $|\mathbf{k}|$ chosen, the overlap from the neighbor WOs in (52) is invisible.

in Eq. (29). For the same reason, the selection rule derived in Sec. II B of paper II [1] that ARPES sees the lower band in the first and the higher band in the second zone is better obeyed for the xy bands than for the (occupied) lower xz and yz bands (compare Figs. 2 and 3 in paper II).

With the knowledge that the right-hand panel of Fig. 5 shows the WO $xy(\mathbf{r})$, let us now imagine building the 1D Bloch sum $xy(k_b\mathbf{b}^*, \mathbf{r})$ of WOs (8) through integer translations by $n\mathbf{b}$, multiplication by $e^{2\pi ink_b}$, and superposition: Around Mo1 and Mo5, only $xy(\mathbf{r})$ contributes (neglecting the tail outside the 70% contour), but around Mo2 and Mo4, $xy(\mathbf{r} + \mathbf{b})e^{-2\pi ik_b}$ and $xy(\mathbf{r} - \mathbf{b})e^{2\pi ik_b}$ also contribute. As a result, at the bottom of the band ($k_b = 0$) the amplitudes around Mo1 and Mo4 are nearly equal, and antibonding between Mo1 and Mo4, whereas the amplitude around Mo2 is smaller, but also antibonding to Mo1 so that the $p\pi$ character on all four oxygens vanishes. At the Fermi level, $|k_b| = 1/4$, whereby the *sum* of the Bloch waves with positive and negative k_b has the same shape as $xy(\mathbf{r})$ near Mo1 and Mo5, and a node at the neighboring Mo1 and Mo5 (i.e., those translated by $\pm\mathbf{b}$). This is the standing-wave state described in the previous section. The shape of the *difference* between the waves with k_b positive and negative is the same, but shifted by \mathbf{b} . At the top of the band, $|k_b| = 1/2$, whereby the Bloch waves change sign upon translation by \mathbf{b} so that there is a node through Mo2 and Mo4 for one of the linear combinations, and through Mo1 and Mo5 for the other. If we finally build the Bloch sums with $|k_b| = 3/4$, we find that they are *identical*

with those for $|k_b| = 1/4$, because in order to form both the low-energy Mo1-Mo4 bonding and the high-energy antibonding states, we would need a set containing *two* xy WOs, one centered at Mo1 and the other at Mo4. In order for a *single* WO to describe the lower bonding part of a 4-eV-wide band, gapped in the middle by merely 0.6 eV, it must in order to reproduce the strong curvature at the top of the lower band at $|k_b| = 1/2$ have the zone boundary (ZB) here (rather than at 1), as well as long-range in the direction (b) of the dispersion. That the latter is not seen in the first panel on the bottom row of Fig. 9 is due to our contour cutoff at 70%. But in the Hamiltonian [Eqs. (35), (37), and (43)], it gives rise to xy - xy hopping integrals τ_n , which we need to carry as far as to $n = 12$.

For future first-principles studies enabling Mott localization onto Mo1 or Mo4, WO sets larger than the one of six used in the present papers will be needed.

In a similar way, we can imagine building the states of the two 1D yz bands (27)–(29) from pseudo-Bloch sums of the yz and YZ WOs (Figs. 5 and 9) through pseudo translations by $n(\mathbf{c} + \mathbf{b})/2$, multiplication by $e^{\pi in(k_c + k_b)}$, and superposition. These WOs have their proper positions, i.e., at, respectively Mo1 and MO1,¹⁴ and we use $yz(\mathbf{r} - n\frac{\mathbf{c} + \mathbf{b}}{2})$ for n even and $YZ[\mathbf{r} - (n - 1)\frac{\mathbf{c} + \mathbf{b}}{2}]$ for n odd; see Eq. (17) and also Eq. (52) to which we shall return. These WOs are so localized that each one spills over only to its neighboring \mathbf{y} string. The integrals for intra- and inter-bi-ribbon hops, $A_1 \pm G_1$, whose complicated hopping paths between elemen-

tary, dressed yz orbitals were shown in (26), are simply those between nearest-neighbor yz and YZ WOs. All farther-ranged hopping integrals, $A_{n>1}$ and $G_{n>1}$, are negligible.

The square of a WO, summed over all lattice translations yields the charge density obtained by filling that band, provided that we neglect its hybridization with the other bands. Summing this charge density over all six WOs yields the charge density obtained by filling all six t_{2g} bands, hybridizations now included. As an example, squaring the xy WO in Fig. 5 will remove the colors and enhance the density on Mo1 with respect to that on the two Mo4 atoms, and even more with respect to that on the two Mo2 atoms, and mostly with respect to that on Mo5. Translating this charge density by $\pm \mathbf{b}$ and summing, doubles the charge density on Mo4 and on Mo2 due to overlap. As a result, the charge density on Mo1 and Mo4 will be nearly equal and larger than that on Mo2, while the one on Mo5 will be the smallest.

This charge density compares well with the one obtained by Popovic and Satpathy [27] for the quasi-1D band by filling it in a narrow range around the Fermi level and shown in the plane of the lower ribbon in their Fig. 5.²⁰

Nuss and Aichhorn [21] described the *four* lowest bands, i.e., the two valence bands and the two metallic bands, with a set of maximally localized Wannier functions obtained numerically by minimizing the spread $\langle \chi | |\mathbf{r} - \mathfrak{R}|^2 | \chi \rangle$.

²⁰That their [27] density on Mo2 is smaller than the one on Mo5 is presumably due to an erroneous exchange of the labels Mo1 and Mo4.

Their WFs are bond centered and are essentially our $yz(\mathbf{r}) + YZ(\mathbf{r})$, our $xz(\mathbf{r}) + XZ(\mathbf{r})$, and a WF along each $\backslash_{\text{Mo1}}/\text{Mo4}\backslash_{\text{Mo1}}/\text{Mo4}\backslash$ chain with xy -like, similar-sized contours on all four sites, smaller contours on the Mo2 and Mo5 sites closest to the bond, and even smaller contours on the next Mo2 and Mo5 sites. This WF is extended along the chain, but appears from their Fig. 4 to have about the same degree of localization as our disk-shaped WO seen in the first column of Fig. 9.

VI. SIX-BAND t_{2g} TIGHT-BINDING HAMILTONIAN

Since our TB Hamiltonian is considerably more detailed than those previously published [6,19,27,28], we have been forced to change *notation*. The relation between the earlier notation and ours is, first of all, $t_{\perp} = t_1 + u_1$ and $t'_{\perp} = t_1 - u_1$. The integral $t \approx -1$ eV for the Mo1-Mo4 hopping used in the earlier work—as well as in the previous sections—is the coefficient of $\cos \pi k_b$, whereas τ_n to be used in Eq. (36) and in the following is the coefficient of $\cos 2\pi n k_b$. The symbol t will from *now* on—unless with explicit reference to Eq. (23)—denote the *function* of k_b and k_c which is defined in terms of the *perpendicular* first- and second-nearest hopping integrals t_1 and t_2 in Eq. (37).

A. Sublattice $\{\mathbf{w}, \mathbf{W}\}$ representation

In the representation of the six Bloch sums (8) of the three Mo1-centered t_{2g} WOs,¹⁴ $w_m(\mathbf{k}, \mathbf{r}) = xy(\mathbf{k}, \mathbf{r})$, $xz(\mathbf{k}, \mathbf{r})$, and $yz(\mathbf{k}, \mathbf{r})$, as well as of the three MO1-centered WOs times a common phase factor, $W_m(\mathbf{k}, \mathbf{r})e^{\pi i(k_c + k_b)} = XY(\mathbf{k}, \mathbf{r})e^{\pi i(k_c + k_b)}$, $XZ(\mathbf{k}, \mathbf{r})e^{\pi i(k_c + k_b)}$, and $YZ(\mathbf{k}, \mathbf{r})e^{\pi i(k_c + k_b)}$, the TB Hamiltonian (9) is

H	xy	XY	xz	XZ	yz	YZ
xy	τ	$t - iu$	$\alpha + i\gamma$	$a - ig$	$\bar{\alpha} + i\bar{\gamma}$	$\bar{a} - i\bar{g}$
XY	$t + iu$	τ	$a + ig$	$\alpha - i\gamma$	$\bar{a} + i\bar{g}$	$\bar{\alpha} - i\bar{\gamma}$
xz	$\alpha - i\gamma$	$a - ig$	0	$A - iG$	$\lambda - i\mu$	$l - im$
XZ	$a + ig$	$\alpha + i\gamma$	$A + iG$	0	$l + im$	$\lambda + i\mu$
yz	$\bar{\alpha} - i\bar{\gamma}$	$\bar{a} - i\bar{g}$	$\lambda + i\mu$	$l - im$	0	$\bar{A} - i\bar{G}$
YZ	$\bar{a} + i\bar{g}$	$\bar{\alpha} + i\bar{\gamma}$	$l + im$	$\lambda - i\mu$	$\bar{A} + i\bar{G}$	0

(35)

using simplified labeling of the rows and columns. The six WOs are real-valued and shown in Fig. 9. The common \mathbf{k} -dependent phase factor $e^{\pi i(k_c + k_b)}$ multiplying the Bloch sums of the upper-string WOs has been included in order that matrix elements between the two different sublattices take the simple form (35) where the asymmetry between integrals for hopping inside and outside a bi-ribbon (electronic dimerization) is given by the imaginary part.

The zero of energy is chosen as the common energy of the xz , XZ , yz , and YZ WOs.

The quantities in (35) named by Greek and Latin letters are real-valued *functions* of the Bloch vector (11). Specifically,

$$\tau(k_b) = \tau_0 + \sum_{n=1}^{12} 2\tau_n \cos 2\pi n k_b, \quad (36)$$

$$t(\mathbf{k}) = (2t_1 \cos \pi k_b + 2t_2 \cos 3\pi k_b) 2 \cos \pi k_c, \quad (37)$$

$$u(\mathbf{k}) = (2u_1 \cos \pi k_b + 2u_2 \cos 3\pi k_b) 2 \sin \pi k_c,$$

describe the xy and XY bands,

$$A(\mathbf{k}) = 2A_1 \cos \pi(k_c - k_b), \quad (38)$$

$$G(\mathbf{k}) = 2G_1 \sin \pi(k_c - k_b)$$

describe the xz and XZ bands, and \bar{A} and \bar{G} describe the yz and YZ bands. An *overbar* is generally used when switching from an xz to a yz orbital and indicates the mirror operation $k_b \leftrightarrow -k_b$, e.g., $\bar{a}(k_b, k_c) \equiv a(-k_b, k_c)$. The hybridizations between the xy / XY and the xz / XZ bands are given by the

Bloch sums:

$$\begin{aligned}
\alpha(\mathbf{k}) &= \alpha_0 + 2\alpha_1 \cos 2\pi k_b + 2\alpha_2 \cos 2\pi k_c \\
&\quad + 2\alpha_3 \cos 2\pi(k_c + k_b) + 2\alpha'_3 \cos 2\pi(k_c - k_b), \\
a(\mathbf{k}) &= 2a_1 \cos \pi(k_c - k_b) + 2a'_1 \cos \pi(k_c + k_b) \\
&\quad + 2a_2 \cos \pi(k_c - 3k_b) + 2a'_2 \cos \pi(k_c + 3k_b), \\
\gamma(\mathbf{k}) &= 2\gamma_1 \sin 2\pi k_b + 2\gamma_2 \sin 2\pi k_c \\
&\quad + 2\gamma_3 \sin 2\pi(k_c + k_b) + 2\gamma'_3 \sin 2\pi(k_c - k_b), \\
g(\mathbf{k}) &= 2g_1 \sin \pi(k_c - k_b) + 2g'_1 \sin \pi(k_c + k_b) \\
&\quad + 2g_2 \sin \pi(k_c - 3k_b) + 2g'_2 \sin \pi(k_c + 3k_b), \quad (39)
\end{aligned}$$

and the hybridizations between the xz/XZ and the yz/YZ bands by

$$\begin{aligned}
\lambda(\mathbf{k}) &= \lambda_0 + 2\lambda_1 \cos 2\pi k_b + 2\lambda_2 \cos 2\pi k_c + 2\lambda_3 \cos 2\pi 2k_b, \\
l(\mathbf{k}) &= (2l_1 \cos \pi k_b) 2 \cos \pi k_c, \\
\mu(\mathbf{k}) &= 2\mu_1 \sin 2\pi k_b + 2\mu_3 \sin 2\pi 2k_b, \\
m(\mathbf{k}) &= (2m_1 \cos \pi k_b) 2 \sin \pi k_c. \quad (40)
\end{aligned}$$

The dispersion along \mathbf{a}^* is neglected, and the Bloch sums are truncated for distances exceeding the lattice constant a , which means after the third-nearest neighbors. The long-ranged $\tau(k_b)$ is an exception and will be discussed below. Due to the truncation of hops longer than a , the effective value of k_a is not zero, but the one for which $\cos 2\pi k_a = 0$, i.e., $1/4$. The truncation also means that our LDA TB bands are a bit more wavy and smoother than those obtained from the original LDA NMTO Hamiltonian downfolded in \mathbf{k} space. The A and G sums (38) are converged already after the first-nearest neighbors.

The Greek-lettered Bloch sums are over hops on the *same* sublattice whereby their \mathbf{k} dependence is periodic in the reciprocal lattice spanned by \mathbf{b}^* and \mathbf{c}^* , e.g.,

$$\alpha(k_b, k_c) = \alpha(k_b + M, k_c + N), \quad (41)$$

with M and N being any integer. The Latin-lettered Bloch sums are over hops *between* the Mo1- and MO1-centered sublattices and averaged such that these Bloch sums are periodic in the double zone spanned by $\mathbf{c}^* + \mathbf{b}^*$ and $\mathbf{c}^* - \mathbf{b}^*$ (see Sec. VIB), but change sign upon odd reciprocal-lattice translations, e.g.,

$$a(k_b, k_c) = (-)^{M+N} a(k_b + M, k_c + N). \quad (42)$$

Note the difference between α and a .

The number of parameters entering Eqs. (36)–(40) and whose values are given in Eqs. (43)–(47) below are far more numerous than those few (t , t_\perp , t'_\perp , A_1 , G_1 , and B) used in the simplified description given in Sec. IV; a description which, nevertheless, suffices to understand the CECs and bands measured by ARPES and shown in, respectively, Figs. 10 and 11 in paper II [1]. The LDA low-energy TB bands shown in Fig. 12(a) of paper II together with the occupied bands measured by ARPES (gray circles and black dots) have much more detail, and the surprisingly good agreement between them proves this detail to be real. This is emphasized by the nearly perfect agreement seen in Fig. 12(b) of paper II and obtained by shifting merely the on-site energy τ_0 of the degenerate xy and XY WOs upwards by 100 meV with respect

to the energy of the degenerate xz , XZ , yz , and YZ WOs. In Sec. III E of paper II we shall describe the details of the energy bands while the differences between LDA and ARPES will be in focus of Sec. IV of paper II.

Below, we give the values in meV of the on-site energies and hopping integrals obtained from the first-principles LDA full-potential NMTO calculation (9) together with the (shifted) values and the [ARPES refined] values (see Secs. IV A and IV B in paper II) in those cases where they differ:

$$\begin{array}{lll}
\tau_0 = 47 \text{ (147) [203]}, & & \\
\tau_1 = -422 [-477], & \tau_5 = -11, & \tau_9 = -2, \\
\tau_2 = 47 [87], & \tau_6 = 8, & \tau_{10} = 1, \\
\tau_3 = -31, & \tau_7 = -4, & \tau_{11} = -1, \\
\tau_4 = 17, & \tau_8 = 3, & \tau_{12} = 1,
\end{array} \quad (43)$$

$$\begin{array}{ll}
t_1 = -11, & u_1 = -3, \\
t_2 = -5, & u_2 = 1,
\end{array} \quad (44)$$

$$A_1 = -319, \quad G_1 = -98 [-109], \quad (45)$$

$$\begin{array}{llll}
\alpha_0 = 31, & & & \\
\alpha_1 = 20, & a_1 = -49, & \gamma_1 = 8, & g_1 = 1, \\
\alpha_2 = -5, & a'_1 = -8, & \gamma_2 = -6, & g'_1 = 5, \\
\alpha_3 = 10, & a_2 = -6, & \gamma_3 = 2, & g_2 = -3, \\
\alpha'_3 = -4, & a'_2 = -11, & \gamma'_3 = -4, & g'_2 = -11,
\end{array} \quad (46)$$

$$\begin{array}{ll}
\lambda_0 = -61, & \mu_1 = 7, \\
\lambda_1 = 7, & \mu_3 = -11, \\
\lambda_2 = 22 [15], & l_1 = 20, \\
\lambda_3 = -11 [-5], & m_1 = 12 [6].
\end{array} \quad (47)$$

Subscript 0 indicates an on-site energy which is the energy of the WO in case the two WOs are identical, and an anisotropy energy in case they are different. Further subscripts indicate first-, second-, and third-nearest-neighbor hops.

As mentioned above, the zero of energy is chosen as the common energy of the xz , XZ , yz , and YZ WOs. This is the center of the gap in the approximation that the hybridizations (40) between the xz/XZ and the yz/YZ bands are neglected. In Sec. IV and in footnote 16 this energy was named $E_0 \sim B + 2|A_1|$. The common energy of the xy and XY WOs, i.e., the center of the unhybridized xy bands, is τ_0 with respect to that of the xz , XZ , yz , and YZ WOs.

For our basis containing merely one Mo1- and one MO1 WO, the Fourier series (36) for the dominating k_b dependence of the two half-filled xy bands converges slowly, as explained in Sec. V. For many purposes, it suffices to linearize $\tau(k_b)$ around $k_b = 1/4 \approx k_F$ or $-1/4$:

$$\begin{aligned}
\tau(k_b) &\approx \tau_0 + 2 \sum_{n=1} (-1)^n \tau_{2n} \\
&\quad - \left(|k_b| - \frac{1}{4} \right) 4\pi \sum_{n=0} (-1)^n (2n+1) \tau_{2n+1}. \quad (48)
\end{aligned}$$

With the values given in (43), the upper line of Eq. (48) says that—neglecting FS warping and splitting, i.e., the perpendicular (44) and hybridization (46) integrals—the Fermi level at half filling is

$$E_F \approx \tau\left(\frac{1}{4}\right) = -23(77) [53] \text{ meV} \quad (49)$$

above the center of the gap. According to Eq. (48), this differs from the on-site xy energy, $\tau_0 = 47(147)$ [203] by the alternating sum $2(-\tau_2 + \tau_4 - \dots)$. Hence, the reason why the ARPES-refined value of the Fermi level for half filling is 150 meV below τ_0 —and thereby closer to the center of the gap than the LDA value shifted by 100 meV—is caused by the refinement of the τ_2 value. In Sec. III B of paper III [2], the average k_{Fb} value measured by ARPES at 33 eV is 0.254. The Fermi level is thus approximately $\tau(0.254) = 75$ meV rather than 53 meV above the center of the gap.

The value of the coefficient of $|k_b| - 1/4$ in the lower line of Eq. (48), times b , yields the Fermi velocity at half filling:

$$v_F = 4.0(4.0) [4.6] \text{ eV \AA}. \quad (50)$$

This LDA value is a bit larger than those of Satpathy and Popovic (3.72 eV \AA) [27] and of Nuss and Aichhorn (0.93 $\times 10^5$ m/s = 3.8 eV \AA) [21]. Our ARPES-refined value, which is consistent with Fig. 14(c2) of paper II [1], exceeds the LDA value by 15%. The reasons for this velocity enhancement will be discussed in Sec. III B 2 of paper III. The dimensionless coupling constant used in Ref. [70] has the value

$$e^2/(\pi \hbar v_F) = 1.14 [0.99]. \quad (51)$$

The splitting-and-warping effects neglected above are considered in detail in Secs. II A, II B, and III B in paper III.

Of the matrix elements, $\langle xy_0 | H | xz_n \rangle = \alpha_n \pm \gamma_n$, determining the xz and yz hybridization of the xy bands, α_0 is the crystal-field term, and $\alpha_n \pm \gamma_n$ and $\bar{\alpha}_n \pm \bar{\gamma}_n$ are integrals for hopping between n th-nearest neighbors with the upper sign for forward hopping and the lower sign for backward hopping. Although these Greek-lettered hops are between WOs on the same sublattice, forward and backward hoppings differ because there is no inversion symmetry around Mo1. These energies, except α_0 and α_1 , are small but significant for the detailed k_c dispersion of the xy band near the Fermi level, especially the resonance behavior. The same holds for the Latin-lettered hopping integrals, $\langle xy_0 | H | XZ_n \rangle = a_n \pm g_n$, between WOs on different sublattices, except for a_1 . In paper III, Sec. II B 6 in particular, we shall see that the crystal-field term α_0 and the integral for hopping from xy to an XZ or YZ nearest-neighbor, a_1 , are of major importance.

The matrix elements $\langle xz_0 | H | yz_n \rangle = \lambda_n \pm \mu_n$ and $\langle xz_0 | H | YZ_n \rangle = l_n \pm m_n$ are larger than these, but of minor importance for the xy band near E_F , and we shall neglect them in the two-band Hamiltonian derived in paper III, Sec. II A. They are decisive for the levels near Z where the valence (V) and conduction (C) bands come closest. Since the Bloch sums (40) are badly converged, we found it necessary to truncate the sum and then refine the hopping values, as shown in square brackets in Eqs. (47). This refinement was enabled by the fact that the six-band Hamiltonian (35) simplifies at the points of high symmetry such as Z.

B. Reciprocal sublattice $\{\mathbf{k}, \mathbf{k} + \mathbf{c}^*\}$ representation

In connection with Eqs. (25) and (29), we note that the numerical values of the most important inter-ribbon hoppings have smaller dimerizations than mean values, i.e., $t_1 \pm u_1 \approx -11 \mp 3$ meV for the xy band and $A_1 \pm G_1 \approx -0.3 \mp 0.1$ eV for the xz and yz bands. If such electronic c -axis dimerizations (Sec. III A) are neglected, the energy bands are the dashed bands in Fig. 6 and correspond to all strings being related by primitive translations $(\mathbf{c} + \mathbf{b})/2$ and $(\mathbf{c} - \mathbf{b})/2$, rather than there being two translationally inequivalent strings per primitive cell whose primitive translations are \mathbf{c} and \mathbf{b} . A natural way of describing the proper electronic structure is therefore in terms of basis functions which are *pseudo-Bloch sums* of WOs with respect to this—too short—lattice periodicity. Specifically, in LiPB, a pseudo-Bloch sum is

$$|w; \mathbf{k}\rangle \equiv \frac{1}{\sqrt{2}} \sum_{\mathbf{T}} e^{2\pi i \mathbf{k} \cdot \mathbf{T}} [w(\mathbf{r} - \mathbf{T}) + e^{2\pi i \mathbf{k} \cdot (\mathbf{c} + \mathbf{b})/2} W(\mathbf{r} - \mathbf{T})], \quad (52)$$

where the \mathbf{T} sum is over the proper lattice translations, $w(\mathbf{r})$ is the WO centered on Mo1, taken as the origin of the primitive cell, and $W(\mathbf{r})$ is the WO on MO1, which is at $(\mathbf{c} + \mathbf{b})/2 - \mathbf{d}$. Both $\sum_{\mathbf{T}} e^{2\pi i \mathbf{k} \cdot \mathbf{T}} w(\mathbf{r} - \mathbf{T})$ and $\sum_{\mathbf{T}} e^{2\pi i \mathbf{k} \cdot \mathbf{T}} W(\mathbf{r} - \mathbf{T})$ are proper Bloch sums (8) and, hence, periodic functions of \mathbf{k} in a single zone. However, the \mathbf{k} -dependent phase factor, $e^{\pi i(k_c + k_b)}$, multiplying the second Bloch sum makes this—and herewith the entire pseudo-Bloch sum (52)—a function of \mathbf{k} which is merely *periodic in the double zone*, i.e., on the *sparse* reciprocal lattice spanned by $\mathbf{c}^* + \mathbf{b}^*$ and $\mathbf{c}^* - \mathbf{b}^*$, that is,

$$\begin{aligned} |w; \mathbf{k}\rangle &= |w; \mathbf{k} + M'(\mathbf{c}^* + \mathbf{b}^*) + N'(\mathbf{c}^* - \mathbf{b}^*)\rangle \\ &\equiv |w; \mathbf{k} + M\mathbf{b}^* + N\mathbf{c}^*\rangle, \end{aligned} \quad (53)$$

with M' and N' being any integers, which means with $M + N$ even. Had $W(\mathbf{r})$ not been displaced and inverted as described in Sec. III A, the pseudo-Bloch sum (52) would have been a proper Bloch sum for the *undimerized* crystal. In Fig. 6, the energy bands of the even pseudo-Bloch sums are the dashed blue, green, and red bands with bottoms near $k_c = 0$.

The correct long periodicity in real space—and *single-zone* periodicity in reciprocal space—can now be described by including in the basis set the pseudo-Bloch sum with \mathbf{k} translated to the *other* sparse sublattice (we may think of reciprocal space as a checkerboard consisting of first and second zones). This second set of Bloch waves¹⁷ is thus $|w; \mathbf{k} + \mathbf{c}^*\rangle$, for which $M + N + 1$ is even, i.e., $M + N$ is *odd*. Their energy bands are the dashed ones with bottoms near $k_c = \pm 1$ (and tops near $k_c = 0$) in Fig. 6. Finally, in order to diagonalize the Hamiltonian (56), the even and odd pseudo-Bloch sums with the same value of \mathbf{k} are allowed to mix and the bands to gap. In absence of dimerization, the even and odd pseudo-Bloch functions are identical, apart from a phase factor, and so are the even and odd energy bands which are merely separated by \mathbf{c}^* and cross without gapping (Fig. 6).

The basis set ($|w; \mathbf{k}\rangle$, $|w; \mathbf{k} + \mathbf{c}^*\rangle$) of pseudo-Bloch sums is simply the unitary transformation:

$$\begin{aligned} |w; \mathbf{k}\rangle &= [w(\mathbf{k}, \mathbf{r}) + e^{\pi i(k_c + k_b)} W(\mathbf{k}, \mathbf{r})]/\sqrt{2}, \\ |w; \mathbf{k} + \mathbf{c}^*\rangle &= [w(\mathbf{k}, \mathbf{r}) - e^{\pi i(k_c + k_b)} W(\mathbf{k}, \mathbf{r})]/\sqrt{2}, \end{aligned} \quad (54)$$

of the set $(w(\mathbf{k}, \mathbf{r}), W(\mathbf{k}, \mathbf{r}))$ of proper Bloch sums (8) of the two WOs $w(\mathbf{r})$ and $W(\mathbf{r})$. We may check that translation of \mathbf{k} by \mathbf{c}^* exchanges the functions on the left-hand side, leaves the proper Bloch functions on the right-hand side invariant, and—by adding one to k_c —changes sign for the second row of the matrix, which correctly exchanges its columns. With the common phase factor $e^{\pi i(k_c+k_b)}$ included in the definition of $W(\mathbf{k}, \mathbf{r})$ as done for the Hamiltonian (35) in the $\{w, W\}$ representation, the transformation (54) is simply the bonding-

antibonding transformation for each of the three t_{2g} Bloch orbitals, and the inverse transformation is

$$w(\mathbf{k}, \mathbf{r}) = [|w; \mathbf{k}\rangle + |w; \mathbf{k} + \mathbf{c}^*\rangle]/\sqrt{2},$$

$$e^{\pi i(k_c+k_b)}W(\mathbf{k}, \mathbf{r}) = [|w; \mathbf{k}\rangle - |w; \mathbf{k} + \mathbf{c}^*\rangle]/\sqrt{2}. \quad (55)$$

Transformed to this $\{|\mathbf{k}, \mathbf{k} + \mathbf{c}^*\rangle\}$ representation, the six-band Hamiltonian (35) becomes

H	$ xy; \mathbf{k}\rangle$	$ xy; \mathbf{k} + \mathbf{c}^*\rangle$	$ xz; \mathbf{k}\rangle$	$ xz; \mathbf{k} + \mathbf{c}^*\rangle$	$ yz; \mathbf{k}\rangle$	$ yz; \mathbf{k} + \mathbf{c}^*\rangle$
$\langle xy; \mathbf{k} $	$\tau + t$	iu	$\alpha + a$	$i(\gamma + g)$	$\bar{\alpha} + \bar{a}$	$i(\bar{\gamma} + \bar{g})$
$\langle xy; \mathbf{k} + \mathbf{c}^* $	$-iu$	$\tau - t$	$i(\gamma - g)$	$\alpha - a$	$i(\bar{\gamma} - \bar{g})$	$\bar{\alpha} - \bar{a}$
$\langle xz; \mathbf{k} $	$\alpha + a$	$-i(\gamma - g)$	A	iG	$\lambda + l$	$-i(\mu - m)$
$\langle xz; \mathbf{k} + \mathbf{c}^* $	$-i(\gamma + g)$	$\alpha - a$	$-iG$	$-A$	$-i(\mu + m)$	$\lambda - l$
$\langle yz; \mathbf{k} $	$\bar{\alpha} + \bar{a}$	$-i(\bar{\gamma} - \bar{g})$	$\lambda + l$	$i(\mu + m)$	\bar{A}	$i\bar{G}$
$\langle yz; \mathbf{k} + \mathbf{c}^* $	$-i(\bar{\gamma} + \bar{g})$	$\bar{\alpha} - \bar{a}$	$i(\mu - m)$	$\lambda - l$	$-i\bar{G}$	$-\bar{A}$

(56)

where $|m; \mathbf{k}\rangle \equiv |w_m; \mathbf{k}\rangle$.

The 3×3 blocks $\langle \mathbf{k}|H|\mathbf{k}\rangle$ and $\langle \mathbf{k} + \mathbf{c}^*|H|\mathbf{k} + \mathbf{c}^*\rangle$ are real-valued, symmetric, and periodic in, respectively, the even and the odd sublattice. This means that $\langle \mathbf{k} + \mathbf{c}^*|H|\mathbf{k} + \mathbf{c}^*\rangle$ equals $\langle \mathbf{k}|H|\mathbf{k}\rangle$ with the sign in front of the Latin-lettered Bloch sum flipped [see Eq. (42)]. The off-diagonal blocks $\langle \mathbf{k}|H|\mathbf{k} + \mathbf{c}^*\rangle$ are caused by the c -axis dimerizations and are purely imaginary.

The band structure with the c -axis dimerizations neglected, consists of the three eigenvalues of the $\langle \mathbf{k}|H|\mathbf{k}\rangle$ block in the double zone ($|k_c| \leq 1$). The dimerization effects may be included by translating these three *undimerized* bands (dashed in Fig. 6) by -1 along k_c , whereby the second BZ ($1/2 \leq k_c \leq 3/2$) falls on top of the first ($-1/2 \leq k_c \leq 1/2$), and finally split them by $\langle \mathbf{k}|H|\mathbf{k} + \mathbf{c}^*\rangle$.

In the following, we shall keep the c -axis dimerizations but often neglect the mm' hybridizations.

C. Pure- m bands

The xy (red), xz (blue), and yz (green) bands drawn in full lines in Fig. 6 have the hybridizations between them neglected. They are the so-called *pure- m* bands, the eigenvalues of the three 2×2 blocks H_m along the diagonal in Eq. (35) or (56), with elements given as functions of k_b and k_c in Eqs. (36)–(38) and numerical values in Eqs. (44) and (45). The pure- yz band we already met in Eq. (29). Note that t , A , and \bar{A} are negative in the first zone and that u , G , and \bar{G} are negative in the positive half of the first zone because nearest-neighbor hopping integrals are negative. After subtraction from H_{xy} of the diagonal $\tau(k_b)$ term, all three blocks have the same form (traceless and Hermitian) and so do, therefore, their upper ($j = 2$) and lower ($j = 1$) eigenvalues:

$$\pm\sqrt{A^2 + G^2}, \quad \pm\sqrt{\bar{A}^2 + \bar{G}^2}, \quad \text{and} \quad \pm\sqrt{t^2 + u^2}, \quad (57)$$

for $m = xz$, yz , and xy , respectively. Similarly for the orthonormal eigenfunctions expressed in terms of the WO Bloch sums used as a basis in Eq. (35), or of the WO pseudo-Bloch

sums used in Eq. (56):

$$w_1(\mathbf{k}, \mathbf{r}) = \frac{1}{\sqrt{2}} [w(\mathbf{k}, \mathbf{r})e^{-i\phi(\mathbf{k})} \mp W(\mathbf{k}, \mathbf{r})e^{\pi i(k_c+k_b)}] \quad (58)$$

$$= \frac{1}{2} \left[|w; \mathbf{k}\rangle (e^{-i\phi(\mathbf{k})} \mp 1) + |w; \mathbf{k} + \mathbf{c}^*\rangle (e^{-i\phi(\mathbf{k})} \pm 1) \right], \quad (59)$$

where

$$e^{i\phi} \equiv \frac{-A - iG}{\sqrt{A^2 + G^2}}, \quad \frac{-\bar{A} - i\bar{G}}{\sqrt{\bar{A}^2 + \bar{G}^2}}, \quad \text{and} \quad \frac{-t - iu}{\sqrt{t^2 + iu^2}}. \quad (60)$$

For quasi-1D structures such as LiPB, the band-structure phase $\phi(\mathbf{k})$ varies from zero at the center of the physical zone (see Sec. VID) to $+\pi/2$ ($-\pi/2$) at the right (left) zone boundaries (ZBs), and to $\pm\pi$ at the centers of the second zones.

From Eq. (59) we see that the $|\mathbf{k}\rangle$ characters of the upper and lower m bands—shown in Fig. 6 as *fatness* added to the respective band dispersions and computed by perturbing the $\langle m; \mathbf{k}|H|m; \mathbf{k}\rangle$ element in the matrix (56) by a small constant energy—are

$$\left| \frac{e^{-i\phi(\mathbf{k})} \mp 1}{2} \right|^2 = \frac{1 \mp \cos \phi(\mathbf{k})}{2} \equiv f_1^2(\mathbf{k}), \quad (61)$$

and these are the same as the $|\mathbf{k} + \mathbf{c}^*\rangle$ characters of the other bands. In Fig. 10, the solid dark and light curves give the $|\mathbf{k}\rangle$ character of, respectively, the lower and upper xy bands as function of k_c in the double zone and along the same line ($k_b = 0.225$) as in Fig. 6. We see the dominant $|\mathbf{k}\rangle$ character switch from the lower band in the first zone to the upper band in the second zone over a range of k_c around the zone boundary (ZB), $|k_c| = 1/2$. On ϕ scale (60), the switching behavior is independent of m and is given by Eq. (61), which says that the interval around the ZB, $|\phi| = \pi/2$, where the $|\mathbf{k}\rangle$ character of *both* bands exceeds, e.g., $1/7 \approx 14\%$, is $\phi = (0.5 \pm 0.253)\pi$. For the two xy bands and $k_b = 0.225$, this “overlap interval” obtained from the third Eq. (60) with Eqs. (37) and (44) is $k_c = (0.35|0.65)$. Had there been no electronic dimerization,

i.e., if u or $G = 0$, the switching curves (Fig. 10) would have been meandering with vertical steps of size 1 at the zone boundaries where the two m bands would have crossed without gapping and could have been folded out to a single m band in the double zone.

The switching curves for the two xy bands along lines of constant k_b are the same for both signs of k_b , and while they always cross at the zone boundary, the steepness of their steps decreases with increasing $|k_b|$ [see Eqs. (37) and (38), and the second column of Chart (1) of paper II for $\kappa_a = 6.4$ and $|k_b| = 0.225, 0.250, \text{ and } 0.275$].

In contrast with the complementarity of the $|\mathbf{k}|$ and $|\mathbf{k} + \mathbf{c}^*$ characters exhibited by Eq. (59), the w and W characters are 50% for both bands and all \mathbf{k} , as seen from Eq. (58).

Bands with different m do hybridize with each other: the $xy(\mathbf{k})$ band with the $xz(\mathbf{k})$ and $yz(\mathbf{k})$ bands due to the α and a hops, and with the $xz(\mathbf{k} + \mathbf{c}^*)$ and $yz(\mathbf{k} + \mathbf{c}^*)$ due to the γ and g hops. The $xz(\mathbf{k})$ band hybridizes with the $yz(\mathbf{k})$ band due to the λ and l hops, and with the $yz(\mathbf{k} + \mathbf{c}^*)$ band due to the μ and m hops.

When $|k_b| \approx 1/4 \approx k_F$, the xy bands are situated in the gap between the xz valence and conduction bands and between the yz valence and conduction bands. The hybridization caused by the (α, a) hops in the $|\mathbf{k}|$ -conserving part and by the (γ, g) hops in the $|\mathbf{k}|$ - $|\mathbf{k} + \mathbf{c}^*$ mixing part of the Hamiltonian (56) makes the difference between the red pure xy bands in Fig. 6 and the dark-red hybridized $\tilde{x}\tilde{y}$ bands in Fig. 7. The (γ, g) hops modify the shape of the $\tilde{x}\tilde{y}$ bands but do not significantly extend the switching region around the BZ boundary, $|k_c| = 1/2$, in which the $|\mathbf{k}|$ - $|\mathbf{k} + \mathbf{c}^*$ mixing occurs.

D. Brillouin and physical zones

Bloch functions are characterized by their translational symmetry in reciprocal space and the choice of the primitive cell (zone) is arbitrary as long as it contains each \mathbf{k} point

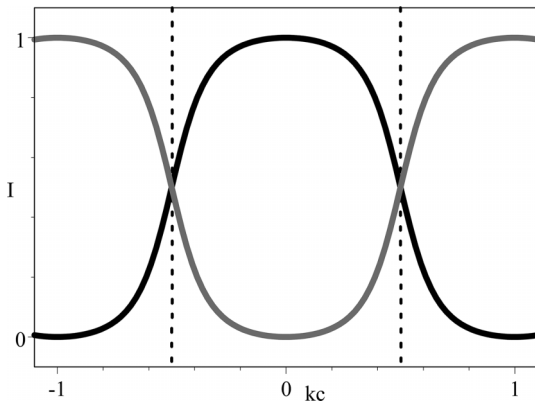


FIG. 10. $|\mathbf{k}|$ character (or relative intensity), $[1 \mp \cos \phi(\mathbf{k})]/2$, of the upper (light) and lower (dark) pure xy bands as functions of k_c for $k_b = 0.225$ in the double zone (Fig. 8); from Eqs. (59), (61), (37), and (44). The dominant (or most intensive) $|\mathbf{k}|$ character switches from the lower band in the odd-numbered zones, $|k_c - 2n| < 1/2$, to the upper band in the even-numbered zones, $|k_c - (2n + 1)| < 1/2$. The gapped bands (57) have single-zone periodicity; their $|\mathbf{k}|$ characters are periodic in the double zone. In Figs. 6 and 7 the $|\mathbf{k}|$ character is shown as fatness added to (i.e., decorating) the band.

once and only once. As we mentioned after Eqs. (29) and (30)–(32), it may be possible and convenient to choose the zone compatible with the electronic structure, i.e., such that gaps occur at the zone boundaries.

For the familiar free-electron model, where $|\mathbf{k}| \sim e^{2\pi i \mathbf{k} \cdot \mathbf{r}}$ and $\varepsilon(\mathbf{k})$ increases isotropically and monotonically with the distance k from $\Gamma(0, 0, 0)$, one chooses that zone which is closer to Γ than to any other point \mathbf{G} of the reciprocal lattice. This is the Brillouin zone (BZ). Application of a weak pseudopotential with crystalline symmetry will couple the basis functions $|\mathbf{k}|$, $|\mathbf{k} - \mathbf{G}_1|$, \dots , and $|\mathbf{k} - \mathbf{G}_n|$, where $\mathbf{G}_1, \dots, \mathbf{G}_n$ are the reciprocal-lattice points closest to Γ , and thereby gap bands where they cross, i.e., where $k = |\mathbf{k} - \mathbf{G}_n|$, which is at the boundaries of the BZ.

For LiPB, the situation is different: Rather than being isotropic, the low-energy electronic structure consists of three pairs of quasi-1D bands. For each, we have only two inequivalent pseudo-Bloch sums, $|w_m; \mathbf{k}|$ and $|w_m; \mathbf{k} + \mathbf{c}^*|$. As described in the previous section and already in the introductory Sec. IV A, and as seen in Figs. 6, 7, and 8 the lower (bonding) m band has $|\mathbf{k}|$ character inside its zone and $|\mathbf{k} + \mathbf{c}^*|$ character outside, while the upper (antibonding) band has $|\mathbf{k} + \mathbf{c}^*|$ character inside and $|\mathbf{k}|$ character outside. Here, “inside” means around a point, such as $\Gamma(k_b = 0, k_c = 0)$, of the even reciprocal sublattice (confusingly called an odd-numbered BZ), and “outside” means around a point, such as $\Gamma(0, 1)$ or $\Gamma(0, -1)$, of the odd reciprocal sublattice (called an even-numbered BZ).

The xz (blue) and yz (green) bands are functions with period two of, respectively, $k_c - k_b$ and $k_c + k_b$ whereby the \mathbf{k} and $\mathbf{k} + \mathbf{c}^*$ bands cross—and gap by $\pm 2G_1$ —along, respectively $|k_c - k_b| = 1/2$ and $|k_c + k_b| = 1/2$, which are then “physical” zone boundaries of the xz and yz bands [Eqs. (32) and (31) and Fig. 8].

The xy bands (red) disperse strongly with k_b , which is normal to the plane of Fig. 6, but since the gap at $|k_b| = 1/2$ caused by b -axis dimerization is far above E_F , we merely consider the two lowest of the four xy bands (see Sec. III B) and their strong k_b dependence is described merely by $\tau(k_b)$. The small $\pm 2u$ gap near E_F is due to the c -axis dimerization (Sec. III A) and occurs at the $|k_c| = 1/2$ zone boundary. Hence, the physical zone for the xy bands is the rectangular one, $[|k_b| \leq 1/2 \text{ and } |k_c| \leq 1/2]$, Eq. (30) which is—actually—the Brillouin zone (BZ).

While the nearly degenerate xy bands are half full (metallic), the lower xz and yz bands are full and the upper bands are empty.

For the purpose of calculating the electronic structure, i.e., when diagonalizing the 6×6 Hamiltonian or the Löwdin downfolded 2×2 Hamiltonian in paper III, we normally use the rectangular BZ.

VII. SUMMARY

In this paper, we have developed the single-particle framework on the basis of which we shall discuss and refine the new ARPES measurements of the band structure and Fermi surface of LiPB to be presented in papers II [1] and III [2].

In the introduction, we gave an overview of the properties and current theories of this intriguing quasi-1D metal and laid

out the plan for—and gave the main results of—our three papers.

In Sec. II, our DFT method for direct computation of Wannier functions and their TB Hamiltonian, the full-potential NMTO method, was explained. Its unique ability to produce physically and chemically meaningful Wannier orbitals (WOs)—multicenter Mo1 $4d$ $t_{2g,m}$ orbitals in the present case—is crucial for our understanding of LiPB whose crystal structure (Fig. 2) consists of MoO₆ octahedra connected via corners into slabs perpendicular to \mathbf{a}^* . Each slab consists of *ribbons*, four molybdenums wide in the $\mathbf{a} + \mathbf{c}$ direction and extending indefinitely in the perpendicular direction, the direction of quasi-1D conductivity [Charts (14) and (15)]. The well-known zigzag chains, $\backslash_{\text{Mo1}}/\text{Mo4}\backslash_{\text{Mo1}}/\text{Mo4}\backslash$, with primitive translation \mathbf{b} , are the spines of the ribbons. The ribbons, with every second *displaced* from the position $(\mathbf{c} + \mathbf{b})/2$ by a vector $-\mathbf{d}$ (16) and *inverted* [Eq. (18) and Chart (14)], are stacked on top of each other into *bi-ribbons*, whereby the slab forms a *staircase* with steps of bi-ribbons and primitive translations \mathbf{c} . Without this c -axis dimerization, the staircase would have been a smooth ramp [Charts (21) and (22)] with the undimerized crystal lattice spanned by $(\mathbf{a}, (\mathbf{c} + \mathbf{b})/2, (\mathbf{c} - \mathbf{b})/2)$ and its reciprocal lattice spanned by $(\mathbf{a}^*, \mathbf{c}^* + \mathbf{b}^*, \mathbf{c}^* - \mathbf{b}^*)$, as compared with the primitive translations $(\mathbf{a}, \mathbf{b}, \mathbf{c})$ and $(\mathbf{a}^*, \mathbf{b}^*, \mathbf{c}^*)$ of real LiPB. The staircase is terminated by insulating MoO₄ tetrahedra and Li intercalates between staircases, which is also where the crystal cleaves. All eight octahedral and four tetrahedral molybdenums approximately form a simple cubic lattice [Eq. (12)].

Anticipating the results of the more technical Secs. V and VI—as well as the band structures and Fermi surface in papers II and III—in Sec. IV we gave an elementary description of the electronic structure inside the slab, from the 10 to the 0.1 eV scale around the Fermi level seen in, respectively, Figs. 3, 4, and 7. The *double zone*, which is the BZ of the undimerized lattice, was shown in Fig. 8. The boundary between the first and second *physical zones*, which is where in the absence of dimerization the $m(\mathbf{k})$ and $m(\mathbf{k} + \mathbf{c}^*)$ bands cross, is shown in solid red, blue, and green lines for $m = xy, xz,$ and yz , respectively. The minimum and maximum of the pure- $m(\mathbf{k})$ band—as well as of the pure- $m(\mathbf{k} + \mathbf{c}^*)$ band—are at the weak lines. The brown dot-dashed line has $k_b = 0.9k_F$ and is the one along which the pure- m bands in Fig. 6 were shown.

The DFT-LDA full-potential NMTO calculations in Sec. V showed that the six lowest-energy bands—half of them occupied—are described by a *set of six* t_{2g} WO per $2\text{LiMo}_6\text{O}_{17}$, namely, $w_m(\mathbf{r})$ centered on Mo1 in the lower ribbon and $W_m(\mathbf{r})$ on the equivalent MO1 in the upper ribbon. These sites, separated by $(\mathbf{c} + \mathbf{b})/2 - \mathbf{d}$, are special in having a full nearest-neighbor shell of octahedral molybdenums and therefore best preserve the t_{2g} symmetry of the WO and are least sensitive to the steps of the staircase. As seen in Figs. 5 and 9, the WO has t_{2g} symmetry around Mo1 (or MO1), and spill over into neighboring atoms which carry *no* WO [see Charts (33) and (34)]. This spillover is necessitated by the requirement that the six Mo1- and MO1-centered t_{2g} WO completely span the wave functions of the six lowest bands and causes what we call a halo on the near atoms.

The xy WO lies inside their respective ribbon and have strong, long-ranged $dd\pi$ intraribbon hopping integrals τ_n

along \mathbf{b} , very weak $dd\delta$ inter-ribbon xy - XY hopping integrals $t_n + u_n$ between partner ribbons, and even weaker $t_n - u_n$ hopping integrals between bi-ribbons [Eqs. (35)–(37), (43), and (44)]. Between slabs, the xy hopping is negligible.¹⁵

The equivalent xz and yz WO stand perpendicular to the ribbons and the $dd\pi$ nearest-neighbor xz - XZ hopping integral, $A_1 + G_1$, between partner ribbons is as strong as the $dd\pi$ intraribbon hopping integral τ_1 between xy orbitals, twice as strong as the hopping integral $A_1 - G_1$ between bi-ribbons [Eqs. (35), (38), and (45)] and 30 times stronger than the $dd\delta$ integrals $t_1 \pm u_1$ for xy - XY hopping. The $A_1 \pm G_1$ integrals are for hopping up or down the staircase with steps $(\mathbf{c} - \mathbf{b})/2$ for xz - XZ and $(\mathbf{c} + \mathbf{b})/2$ for yz - YZ . The two xz bands are gapped by the hopping dimerization $\pm 2G_1 \approx \pm 0.2$ eV and so are the two yz bands (Figs. 6 and 7).

The six-band TB Hamiltonian was given in Eq. (35) in terms of these and further hopping integrals, Bloch summed as in Eq. (8). The basis functions were the Bloch-summed WO, $w_m(\mathbf{k}, \mathbf{r})$ and $e^{\pi i(k_c + k_b)} W_m(\mathbf{k}, \mathbf{r})$ on, respectively, the lower and the upper ribbon, and the \mathbf{k} -dependent phase factor in front of $W_m(\mathbf{k}, \mathbf{r})$ was included to make the electronic dimerizations purely imaginary. Further insight was gained in Sec. VIB by transforming from this basis set—which for each m consists of two Bloch sums, one over the Mo1 positions and the other over the MO1 positions,—to one with two *pseudo*-Bloch sums (52), $|m; \mathbf{k}\rangle \equiv |w_m, \mathbf{k}\rangle$ and $|m; \mathbf{k} + \mathbf{c}^*\rangle$, each of which is a Bloch sum over both Mo1 and MO1 with every second phase factor along \mathbf{c} chosen as $e^{2\pi i \mathbf{k} \cdot [\mathbf{T} + (\mathbf{c} + \mathbf{b})/2]}$, i.e., as if there were no displacement dimerization, $\mathbf{d} = \mathbf{0}$. The transformation is (54). Considered as a function of \mathbf{k} , the pseudo-Bloch sum $|\mathbf{k}\rangle$ is a periodic function on the sparse, so-called *even* reciprocal lattice spanned by $(\mathbf{a}^*, \mathbf{c}^* + \mathbf{b}^*, \mathbf{c}^* - \mathbf{b}^*)$ whose BZ is the *double zone* shown in Fig. 8. Together with the function $|\mathbf{k} + \mathbf{c}^*\rangle$, periodic on the *odd* reciprocal lattice, they form a complete, orthonormal basis set for the proper, dimerized crystal. In the absence of dimerization, $|\mathbf{k}\rangle$ and $|\mathbf{k} + \mathbf{c}^*\rangle$ are identical apart from a phase factor, but they become linearly *independent* in the presence of dimerization and will mix near the boundaries of the appropriate physical zone. The six-band TB Hamiltonian (56) in this so-called $\{|\mathbf{k}\rangle, |\mathbf{k} + \mathbf{c}^*\rangle\}$ representation was used to visualize the $|\mathbf{k}\rangle$ characters of the band structures in Figs. 6 and 7 as their (additional) *fatness* (61). Figure 10 shows how the $|\mathbf{k}\rangle$ characters of the lower and upper m bands switch between zero and one, and back again, as the Bloch vector crosses the boundaries of the physical (m dependent) zone.

In the following paper II [1], we shall find the important result that this interesting $|\mathbf{k}\rangle$ -character variation is experimentally manifested as an ARPES intensity selection rule. As mentioned already in the introduction, when this selection rule is combined with our new ARPES data, it enables the separation of the two bands that disperse to define the FS. In paper III, we will also use the selection rule to reveal the FS features that are peculiar to each of the two bands. Thereby our new ARPES results both confirm and are greatly aided by our theory. But first, at the beginning of paper II, we shall give the complete theory, which includes the distortion of the ARPES intensity variations caused by the c -axis displacement and inversion dimerizations. The latter depends on the photon energy, which we have chosen such that they basically cancel.

ACKNOWLEDGMENTS

We are indebted to Tanusri Saha-Dasgupta, Sashi Satpathy, and Zoran Popovic for their active participation at the initial stage of this project. J.W.A. acknowledges past support of this work by the U.S. National Science Foundation (Grant

No. DMR-07-04480). This research used resources of the Advanced Light Source, which is a DOE Office of Science User Facility under Contract No. DE-AC02-05CH11231. M.G. acknowledges support by the U.S. National Science Foundation (Grant No. DMR-15-07252).

-
- [1] L. Dudy, J. W. Allen, J. D. Denlinger, J. He, M. Greenblatt, M. W. Haverkort, Y. Nohara, and O. K. Andersen, companion paper, *Phys. Rev. B* **109**, 115144 (2024).
- [2] L. Dudy, J. W. Allen, J. D. Denlinger, J. He, M. Greenblatt, M. W. Haverkort, Y. Nohara, and O. K. Andersen, companion paper, *Phys. Rev. B* **109**, 115145 (2024).
- [3] M. Greenblatt, W. McCarroll, R. Neifeld, M. Croft, and J. Waszczak, *Solid State Commun.* **51**, 671 (1984).
- [4] M. Onoda, K. Toriumi, Y. Matsuda, and M. Sato, *J. Solid State Chem.* **66**, 163 (1987).
- [5] L. Dudy, J. D. Denlinger, J. W. Allen, F. Wang, J. He, D. Hitchcock, A. Sekiyama, and S. Suga, *J. Phys.: Condens. Matter* **25**, 014007 (2013).
- [6] J. Merino and R. H. McKenzie, *Phys. Rev. B* **85**, 235128 (2012).
- [7] J. Merino and J. V. Alvarez, *Phys. Rev. B* **91**, 035135 (2015).
- [8] W. Cho, C. Platt, R. H. McKenzie, and S. Raghu, *Phys. Rev. B* **92**, 134514 (2015).
- [9] N. Lera and J. V. Alvarez, *Phys. Rev. B* **92**, 174523 (2015).
- [10] G. Wu, X.-s. Ye, X. Zeng, B. Wu, and W. Clark, *Sci. Rep.* **6**, 20721 (2016).
- [11] C. Platt, W. Cho, R. H. McKenzie, R. Thomale, and S. Raghu, *Phys. Rev. B* **93**, 214515 (2016).
- [12] P. Chudziński, *Eur. Phys. J. B* **90**, 148 (2017).
- [13] J. Lu, X. Xu, M. Greenblatt, R. Jin, P. Tinnemans, S. Licciardello, M. R. van Delft, J. Buhop, P. Chudzinski, and N. E. Hussey, *Sci. Adv.* **5**, eaar8027 (2019).
- [14] S.-i. Tomonaga, *Prog. Theor. Phys.* **5**, 544 (1950).
- [15] J. M. Luttinger, *J. Math. Phys.* **4**, 1154 (1963).
- [16] T. Giamarchi, *Quantum Physics in One Dimension* (Oxford University Press, 2004).
- [17] J. Hager, R. Matzdorf, J. He, R. Jin, D. Mandrus, M. A. Cazalilla, and E. W. Plummer, *Phys. Rev. Lett.* **95**, 186402 (2005).
- [18] D. Orgad, S. A. Kivelson, E. W. Carlson, V. J. Emery, X. J. Zhou, and Z. X. Shen, *Phys. Rev. Lett.* **86**, 4362 (2001).
- [19] P. Chudzinski, T. Jarlborg, and T. Giamarchi, *Phys. Rev. B* **86**, 075147 (2012).
- [20] F. Wang, J. V. Alvarez, S.-K. Mo, J. W. Allen, G.-H. Gweon, J. He, R. Jin, D. Mandrus, and H. Höchst, *Phys. Rev. Lett.* **96**, 196403 (2006).
- [21] M. Nuss and M. Aichhorn, *Phys. Rev. B* **89**, 045125 (2014).
- [22] O. Sepper and A. G. Lebed, *Phys. Rev. B* **88**, 094520 (2013).
- [23] A. G. Lebed and O. Sepper, *Phys. Rev. B* **87**, 100511(R) (2013).
- [24] X. Xu, A. F. Bangura, J. G. Analytis, J. D. Fletcher, M. M. J. French, N. Shannon, N. E. Hussey, J. He, S. Zhang, D. Mandrus, R. Jin *et al.*, *Phys. Rev. Lett.* **102**, 206602 (2009).
- [25] N. Wakeham, A. F. Bangura, X. Xu, J.-F. Mercure, M. Greenblatt, and N. E. Hussey, *Nat. Commun.* **2**, 396 (2011).
- [26] M. H. Whangbo and E. Canadell, *J. Am. Chem. Soc.* **110**, 358 (1988).
- [27] Z. S. Popovic and S. Satpathy, *Phys. Rev. B* **74**, 045117 (2006).
- [28] T. Jarlborg, P. Chudzinski, and T. Giamarchi, *Phys. Rev. B* **85**, 235108 (2012).
- [29] J. A. M. Haverkort, in International Workshop on Strong Correlations and Angle-Resolved Photoemission Spectroscopy (2013), <http://corpes13.xfel.eu/>.
- [30] Y. Nohara and O. K. Andersen, *Phys. Rev. B* **94**, 085148 (2016).
- [31] J. P. Pouget, B. Hennion, C. Escribe-Filippini, and M. Sato, *Phys. Rev. B* **43**, 8421 (1991).
- [32] M.-H. Whangbo, E. Canadell, P. Foury, and J.-P. Pouget, *Science* **252**, 96 (1991).
- [33] J. D. Denlinger, G.-H. Gweon, J. W. Allen, C. G. Olson, J. Marcus, C. Schlenker, and L.-S. Hsu, *Phys. Rev. Lett.* **82**, 2540 (1999).
- [34] K. Breuer, D. M. Goldberg, K. E. Smith, M. Greenblatt, and W. McCarroll, *Solid State Commun.* **94**, 601 (1995).
- [35] U. von Barth and L. Hedin, *J. Phys. C: Solid State Phys.* **5**, 1629 (1972).
- [36] W. Kohn and L. J. Sham, *Phys. Rev.* **140**, A1133 (1965).
- [37] O. K. Andersen and T. Saha-Dasgupta, *Phys. Rev. B* **62**, R16219 (2000).
- [38] R. Tank and C. Arcangeli, *Phys. Status Solidi B* **217**, 89 (2000).
- [39] O. K. Andersen, T. Saha-Dasgupta, R. Tank, C. Arcangeli, O. Jepsen, and G. Krier, *Electronic Structure and Physical Properties of Solids. The Uses of the LMTO Method* (Springer, 2000).
- [40] O. K. Andersen, *Phys. Rev. B* **12**, 3060 (1975).
- [41] O. K. Andersen and O. Jepsen, *Phys. Rev. Lett.* **53**, 2571 (1984).
- [42] E. Pavarini, A. Yamasaki, J. Nuss, and O. K. Andersen, *New J. Phys.* **7**, 188 (2005).
- [43] E. Zurek, O. Jepsen, and O. K. Andersen, *ChemPhysChem* **6**, 1934 (2005).
- [44] A. Yamasaki, M. Feldbacher, Y.-F. Yang, O. K. Andersen, and K. Held, *Phys. Rev. Lett.* **96**, 166401 (2006).
- [45] F. Lechermann, A. Georges, A. Poteryaev, S. Biermann, M. Posternak, A. Yamasaki, and O. K. Andersen, *Phys. Rev. B* **74**, 125120 (2006).
- [46] L. Boeri, G. B. Bachelet, M. Giantomassi, and O. K. Andersen, *Phys. Rev. B* **76**, 064510 (2007).
- [47] G.-Q. Liu, V. N. Antonov, O. Jepsen, and O. K. Andersen, *Phys. Rev. Lett.* **101**, 026408 (2008).
- [48] P. R. C. Kent, T. Saha-Dasgupta, O. Jepsen, O. K. Andersen, A. Macridin, T. A. Maier, M. Jarrell, and T. C. Schulthess, *Phys. Rev. B* **78**, 035132 (2008).
- [49] T. Saha-Dasgupta, O. K. Andersen, J. Nuss, A. Poteryaev, A. Georges, and A. Lichtenstein, [arXiv:0907.2841](https://arxiv.org/abs/0907.2841).
- [50] E. Zurek, O. Jepsen, and O. K. Andersen, *Inorg. Chem. (Washington, DC, U. S.)* **49**, 1384 (2010).
- [51] O. K. Andersen and L. Boeri, *Ann. Phys. (Berlin, Ger.)* **523**, 8 (2011).

- [52] M. W. Haverkort, M. Zwierzycki, and O. K. Andersen, *Phys. Rev. B* **85**, 165113 (2012).
- [53] N. Marzari, A. A. Mostofi, J. R. Yates, I. Souza, and D. Vanderbilt, *Rev. Mod. Phys.* **84**, 1419 (2012).
- [54] www.quanty.org.
- [55] O. K. Andersen, *NMTOs and their Wannier functions, Correlated Electrons: From Models to Materials: Lecture Notes of the Autumn School Correlated Electrons 2012*, Vol. 2 of *Schriften des Forschungszentrums Jülich: Reihe Modeling and Simulation* (Forschungszentrum Jülich, 2012).
- [56] M. Zwierzycki and O. K. Andersen, *Acta Phys. Pol.* **115**, 64 (2009).
- [57] M. Methfessel, M. v. Schilfgaarde, and R. A. Casali, *Electronic Structure and Physical Properties of Solids. The Uses of the LMTO Method* (Springer, 2000).
- [58] J. M. Wills, O. Eriksson, M. Alouani, and D. L. Price, *Electronic Structure and Physical Properties of Solids. The Uses of the LMTO Method* (Springer, 2000).
- [59] J. M. Wills, M. Alouani, P. Andersson, A. Delin, O. Eriksson, and O. Grechnev, *Full-Potential Electronic Structure Method: Energy and Force Calculations with Density Functional and Dynamical Mean Field Theory* (Springer Science & Business Media, 2010), Vol. 167.
- [60] K. Lejaeghere, G. Bihlmayer, T. Björkman, P. Blaha, S. Blügel, V. Blum, D. Caliste, I. E. Castelli, S. J. Clark, A. Dal Corso *et al.*, *Science* **351**, aad3000 (2016).
- [61] O. K. Andersen, O. Jepsen, and G. Krier, *Lectures in Methods of Electronic Structure Calculations* (World Scientific, 1995).
- [62] L. Vitos, *Computational Quantum Mechanics for Materials Engineers: The EMTO Method and Applications* (Springer Science & Business Media, 2007).
- [63] W. R. L. Lambrecht and O. K. Andersen, *Phys. Rev. B* **34**, 2439 (1986).
- [64] E. Zurek, J. Autschbach, and O. K. Andersen, *AIP Conf. Proc.* **963**, 1421 (2007).
- [65] S. Satpathy and Z. Pawłowska, *Phys. Status Solidi B* **145**, 555 (1988).
- [66] W. Ku, H. Rosner, W. E. Pickett, and R. T. Scalettar, *Phys. Rev. Lett.* **89**, 167204 (2002).
- [67] Y. Nohara and O. K. Andersen (unpublished).
- [68] P. Foury and J. Pouget, *Int. J. Mod. Phys. B* **07**, 3973 (1993).
- [69] M. I. Aroyo, D. Orobengoa, G. de la Flor, E. S. Tasci, J. M. Perez-Mato, and H. Wondratschek, *Acta Crystallogr. Sect. A* **70**, 126 (2014).
- [70] P. Kopietz, V. Meden, and K. Schönhammer, *Phys. Rev. Lett.* **74**, 2997 (1995).